science.sciencemag.org/content/368/6492/763/suppl/DC1

Supplementary Materials for

Photocurrent detection of the orbital angular momentum of light

Zhurun Ji, Wenjing Liu, Sergiy Krylyuk, Xiaopeng Fan, Zhifeng Zhang, Anlian Pan,
Liang Feng, Albert Davydov, Ritesh Agarwal*

*Corresponding author. Email: riteshag@seas.upenn.edu

Published 15 May 2020, *Science* **368**, 763 (2020)
DOI: 10.1126/science.aba9192

This PDF file includes:

- Materials and Methods
- Supplementary Text
- Figs. S1 to S19
- Table S1
- References

Materials and Methods

Experimental setup

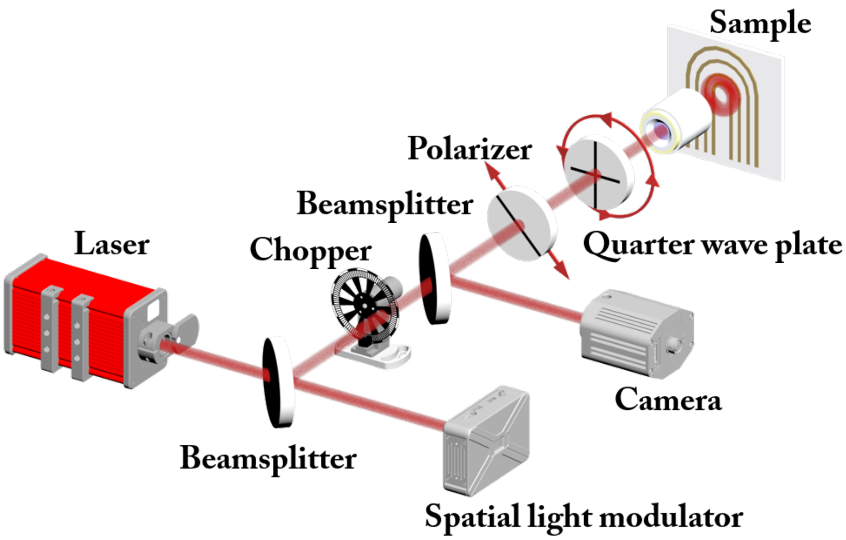

Figure S1: Experimental setup for measuring photocurrent from OAM of light.

Sample growth and device fabrications

WTe_2 single-crystals were grown by the chemical vapor transport (CVT) method using polycrystalline WTe_2 powder (~1 g) and iodine transport agent (5 mg/cm^3) sealed in an evacuated quartz ampoule. The ampoule was ice-water quenched after 7 days of growth at 900 °C.

The 50 ~ 200 nm thick WTe_2 sample flakes were obtained by Polydimethylsiloxane (PDMS) assisted mechanical exfoliation, and Ti/ Au electrodes were post-patterned by Electron beam lithography (EBL) and Physical vapor deposition (PVD) processes. As shown in main text Fig. 2a, the thickness of small electrodes is 50 nm, and large electrodes is ~ 400 nm.

Supplementary Text

1 Theory of the orbital photogalvanic effect (OPGE)

1.1 Description of electromagnetic wave carrying orbital angular momentum

Assuming the electric field of light is $\vec{E}(\vec{r},t)$, magnetic field $\vec{B}(\vec{r},t)$, and vector potential $\vec{A}(\vec{r},t)$, then the total linear momentum carried by the EM wave can be calculated by $\vec{P} = \int \epsilon_0 \vec{E} \times \vec{B} d^3\vec{r}$, and its angular momentum would be the cross product of position vector $\vec{r}$ and $\vec{P}$ *(5)*:

$$\vec{L} = \epsilon_0 \int \vec{r} \times (\vec{E} \times \vec{B}) d^3\vec{r} \tag{S1}$$

It can be further decomposed into two parts, with one part representing orbital angular momentum (OAM) and the other part representing spin angular momentum (SAM). By replacing $\vec{B}$ by $\nabla \times \vec{A}$, and adopting the Coulomb gauge where $\nabla \cdot \vec{A} = 0$, Eqn. S1 can be rewritten as,

$$\vec{L} = \epsilon_0 \int \sum_{j=x,y,z} E_j (\vec{r} \times \nabla) A_j d^3\vec{r} + \epsilon_0 \int (\vec{E} \times \vec{A}) d^3\vec{r} \tag{S2}$$

Considering a monochromatic field in our case $\vec{E} = Re(\vec{\mathcal{E}} e^{(-i\omega t)})$, where $\vec{\mathcal{E}}$ is the amplitude of the electromagnetic field and ω the angular frequency of light. Using $\vec{E} = -\frac{\partial \vec{A}}{\partial t}$ and neglecting the terms oscillating with twice the frequency, one can find that the second term in Eqn. S2,

$$\vec{E} \times \vec{A} \propto Im[\vec{\mathcal{E}} \times \vec{\mathcal{E}}^*] \tag{S3}$$

This term is in fact dependent on the polarization of light, $\vec{e} = \frac{\vec{\mathcal{E}}}{|\vec{\mathcal{E}}|}$, or in other words associated with the light SAM. The circular photogalvanic effect, as described by the dependence of a dc photocurrent on the circular polarization of light, is directly related to this term.

To rewrite the first term, we can use the paraxial approximation, in the small divergence angle limit of the optical beam. We also assume that near the beam focus, the direction of polarization $\vec{e}$ does not change significantly with spatial position (for now). Under these approximations, we get

$$\sum_{j=x,y,z} E_j (\vec{r} \times \nabla) A_j \propto \sum_{j=x,y,z} E_j (\vec{r} \times \nabla) E_j^* \propto \vec{e} \cdot \vec{e} \tag{S4}$$

which means the first term in Eqn. S2 is independent of the polarization direction, but is associated with the spatial distribution of the EM wave. The z-component of the first term in Eqn (S2) now becomes

$$L_z = \frac{\epsilon_0}{2i\omega} \int \sum_{j=x,y,z} (E_j^* \frac{\partial}{\partial \phi} E_j) d^3\vec{r} \tag{S5}$$

Here ϕ is the azimuthal angle in the plane perpendicular to $\hat{\boldsymbol{z}}$, and L_z is the OAM of light.

1.2 Description of the Laguerre-Gaussian modes

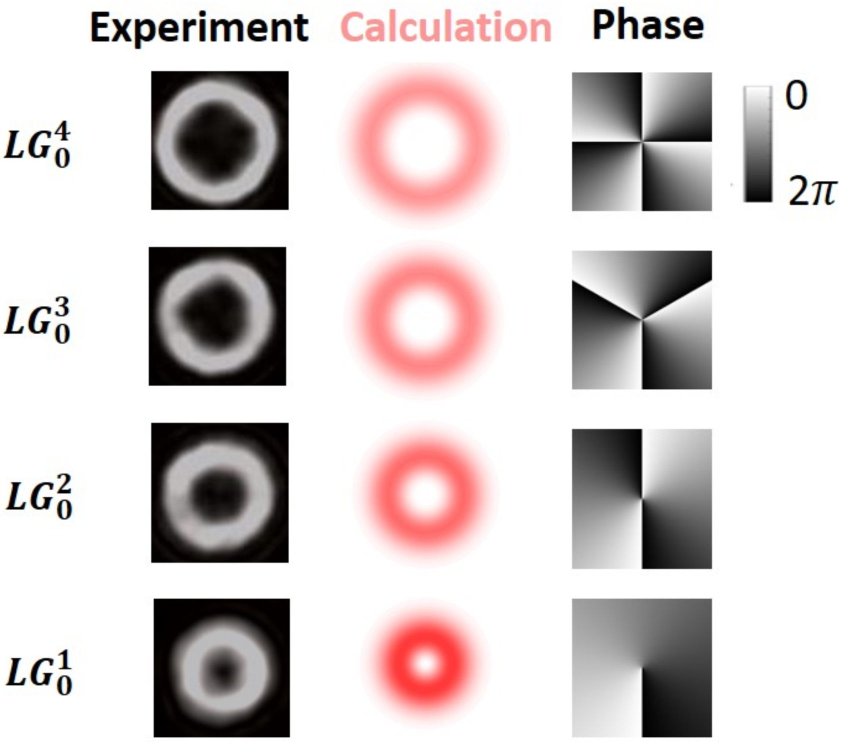

Figure S2: CCD images of LG beams LG_0^1 -LG_0^4 in the experiment, calculated mode profiles, and phase profiles.

In experiments, the scalar OAM beams were obtained by a phase-only spatial light modulator (SLM). The programmable holograms on the SLM (phase profiles) shown in Fig. S2 convert Gaussian beams into Laguerre-Gaussian (LG) modes. The most general description of LG modes is given by *(17)*,

$$u(\rho,\phi,z) = \frac{C_{mp}^{LG}}{w(z)}(\frac{\rho\sqrt{2})}{w(z)})^{|m|}e^{-\frac{\rho^2}{w^2(z)}}L_p^{|m|}(\frac{2\rho^2}{w^2(z)})e^{-ik\frac{\rho^2}{2R(z)}}e^{im\phi}e^{i\psi(z)} \tag{S6}$$

with L_p^m being the generalized Laguerre polynomials and C_{mp}^{LG} the normalization coefficient,

$$C_{mp}^{LG} = \sqrt{\frac{2p!}{\pi(p+|m|)!}} \tag{S7}$$

$w(z) = w_0\sqrt{1+(\frac{z}{z_R})^2}$, $z_R = \frac{\pi w_0^2}{\lambda}$ is called the Rayleigh length, and $e^{im\phi}$ is the conventional we adopted. $R(z) = z[1+(\frac{z_R}{z})^2]$ is the radius of curvature of the beam's wavefront at z and $\psi(z)$ is the Gouy phase. $|u(\rho,\phi,z)|^2$ has a circular symmetry, and the two controlling factors of its shape and phase profile are radial index $p \geq 0$ and azimuthal index m. In our discussion of light OAM, only $p = 0$ beams are considered. Another assumption we made is that the LG beams are focused on the surface of the sample, i.e. $\psi(z) = 0$ (for thin samples). The electric field profile $\mathcal{E}(\rho, \phi, 0) = \mathcal{E}_0 u(\rho, \phi, 0)$ can then be simplified to,

$$\mathcal{E}(\rho, \phi, 0) = \mathcal{E}_0 \sqrt{\frac{2}{\pi |m|!}} \frac{1}{w_0} (\frac{\rho\sqrt{2}}{w_0})^{|m|} e^{-\frac{\rho^2}{w_0^2}} e^{im\phi} \tag{S8}$$

$|\mathcal{E}|^2$ from the CCD image in the experiment and from numerical calculations are plotted in Fig. S2. These beams each carry a well defined OAM of $m\hbar$ per photon. Due to the phase singularity when $m \neq 0$, the beam intensity at $\rho = 0$ vanishes. The ring distance defined by the distance between the center of the LG beam and the point it reaches its intensity maxima would be $\rho_0 = \sqrt{\frac{|m|}{2}} w_0$.

To summarize, LG beams have two main characteristics:
1. LG_0^m beams have circular symmetric intensity distributions and their phases varies along the azimuthal direction.
2. LG_0^m beams have the same intensity distribution as LG_0^{-m}, but with an opposite phase, $m\phi$ and $-m\phi$. For different m numbers, they have different intensity as well as phase distribution.

1.3 A general expression of second order susceptibilities

Two arbitrary incident electric fields, $E_1(\boldsymbol{r}, t)$ and $E_2(\boldsymbol{r}, t)$, can be Fourier expanded in the frequency and momentum space as,

$$E_1(\boldsymbol{r}, t) = \frac{1}{(2\pi)^4} \iint d\boldsymbol{q_1} d\omega_1 E_1(\boldsymbol{q}_1, \omega_1) e^{-i\omega_1 t + i\boldsymbol{q}_1 \cdot \boldsymbol{r}} \tag{S9}$$

$$E_2(\boldsymbol{r}, t) = \frac{1}{(2\pi)^4} \iint d\boldsymbol{q_2} d\omega_2 E_2(\boldsymbol{q}_2, \omega_2) e^{-i\omega_2 t + i\boldsymbol{q}_2 \cdot \boldsymbol{r}} \tag{S10}$$

A general second order response reads,

$$j_k^{(2)}(\boldsymbol{r}, t) = \int \frac{d\boldsymbol{q}_1 d\omega_1 d\boldsymbol{q}_2 d\omega_2}{(2\pi)^8} e^{-i(\omega_1+\omega_2)t} e^{i(\boldsymbol{q}_1+\boldsymbol{q}_2)\cdot\boldsymbol{r}} \xi_{ijk}(\boldsymbol{q}_1, \omega_1; \boldsymbol{q}_2, \omega_2) \\ E_{1,i}(\boldsymbol{q}_1, \omega_1) E_{2,j}(\boldsymbol{q}_2, \omega_2) \tag{S11}$$

Here the subscripts i, j and k denote the axes in the Cartesian coordinate, 1, 2 are the dummy indices for representation of frequency components, and $\xi_{ijk}(\boldsymbol{q}_1, \omega_1; \boldsymbol{q}_2, \omega_2)$ is a third rank conductivity tensor. The tensor is symmetric in its components in the way that,

$$\xi_{ijk}(\boldsymbol{q}_1, \omega_1; \boldsymbol{q}_2, \omega_2) = \xi_{ijk}^{(1)}(\boldsymbol{q}_1, \omega_1; \boldsymbol{q}_2, \omega_2) + \xi_{jik}^{(2)}(\boldsymbol{q}_2, \omega_2; \boldsymbol{q}_1, \omega_1) \tag{S12}$$

For the case of monochromatic waves (i.e., $E(t) = Ee^{-i\omega t} + c.c.$), and in the small $\boldsymbol{q}$ perturbation limit (this expansion is reasonable given the small linear momentum per photon compared to that of the charge carriers ($\sim 10^{-3}$)), the conductivity tensor can be expanded up to the first order of $\boldsymbol{q}$ as,

$$\xi_{ijk}(\boldsymbol{q}_1,\omega_1;\boldsymbol{q}_2,\omega_2)=\alpha_{ijk}(\omega_1,\omega_2)+q_{1,l}\eta_{ijkl}(\omega_1,\omega_2)+q_{2,l}\eta_{jikl}(\omega_2,\omega_1) \tag{S13}$$

Where α_{ijk} is a zeroth order in $\boldsymbol{q}$ conductivity (susceptibility) tensor, which well describes the limit of electric field being homogeneous in space (i.e., $E(\boldsymbol{r})=E(\boldsymbol{r_0})$). On the other hand, η_{jikl} is a first order in $\boldsymbol{q}$ conductivity tensor and describes the *nonlocal* second order effects in a system. Since η_{ijkl} is a fourth rank tensor, it has different symmetry selection rules comparing to α_{ijk}, e.g., it could be nonzero under inversion symmetry. Below we denote the first order in $\boldsymbol{q}$ part of conductivity tensor as $\xi^{(1)}$, and the corresponding dc photocurrent response as $j^{(dc,(1))}$.

According to the properties of momentum $\boldsymbol{q}$, a nonlocal effect may arise from the intensity gradient of the beam (s-PGE) *(21)*, from the photon wave vector (photon drag effect) *(26)*, or alternatively from the photon orbital angular momentum (denoted as OPGE) as discussed in this paper. Below we will explain these three effects in detail:

(1) **Spatially dispersive photogalvanic effect (s-PGE)**

When the non-locality in a system is from the intensity inhomogeneity of the optical beam, the complex electric field amplitude in the Fourier space follows $E(\boldsymbol{q},-\omega)=E^*(\boldsymbol{q},\omega)$, and in the real space,

$$E(\boldsymbol{r},t)=\frac{1}{(2\pi)^4}\iint d\boldsymbol{q}d\omega(E(\boldsymbol{q},\omega)e^{-i\omega t}+E(\boldsymbol{q},-\omega)e^{i\omega t})e^{i\boldsymbol{q}\cdot\boldsymbol{r}} \tag{S14}$$

The dc current conductivity (from ω, $-\omega$ interaction) can then be written as,

$$\xi^{(1)}_{ijk}(\boldsymbol{q},\omega;\boldsymbol{q},-\omega)=q_l\eta_{ijkl}(\omega,-\omega)+q_l\eta_{jikl}(-\omega,\omega) \tag{S15}$$

and in real space,

$$\begin{aligned} j^{(dc,(1))}_k(\boldsymbol{r},t)=\int &\frac{d\boldsymbol{q}d\omega d\boldsymbol{q}d(-\omega)}{(2\pi)^8}e^{-i(\omega-\omega)t}e^{i(\boldsymbol{q}+\boldsymbol{q})\cdot\boldsymbol{r}} \\ &\cdot\xi^{(1)}_{ijk}(\boldsymbol{q},\omega;-\boldsymbol{q},-\omega)E_i(\boldsymbol{q},\omega)E_j(\boldsymbol{q},-\omega) \end{aligned} \tag{S16}$$

This effect is called the spatially dispersive photogalvanic effect since it generates a photocurrent from the spatial dispersion of light intensity, and it exists in any system going beyond the plane wave approximation. A generic example is the Gaussian beam, which has an intensity gradient in the radial direction, $I(\rho)\propto e^{-\rho^2/r_0^2}$.

For a Laguerre-Gaussian beam, the intensity gradient is determined by its mode profile $\mathcal{E}(\rho,\phi,0)$.

$$\mathcal{E}(\rho,\phi,0)=\mathcal{E}_0\sqrt{\frac{2}{\pi|m|!}}\frac{1}{w_0}(\frac{\rho\sqrt{2}}{w_0})^{|m|}e^{-\frac{\rho^2}{w_0^2}}e^{-im\phi} \tag{S17}$$

The intensity gradient is then,

$$\frac{\partial|\mathcal{E}(\rho,\phi,0)|^2}{\partial r}=\mathcal{E}_0^2\frac{2}{\pi|m|!}\frac{1}{w_0^2}\{|2m|(\frac{\sqrt{2}}{w_0})^{|2m|}\rho^{|2m|-1}-\frac{2\rho}{w_0^2}(\frac{\rho\sqrt{2}}{w_0})^{|2m|}\}e^{-\frac{2\rho^2}{w_0^2}} \tag{S18}$$

The s-PGE current has a direct dependence on the intensity gradient.

(2) **Photon drag effect**

A simple interpretation of photon drag effect is the transfer of linear momentum from photon to the electron, leading to asymmetric excited carrier population in the momentum space, generating a second order dc photocurrent. This dc photocurrent, second order in an electric field $\boldsymbol{E}=\boldsymbol{E_0}e^{i\boldsymbol{k}\cdot\boldsymbol{r}}$, is proportional to $\boldsymbol{k}$, the wave vector of the beam. To be specific, the complex electric field amplitude in the Fourier space has $E(\boldsymbol{q},-\omega)=E^*(-\boldsymbol{q},\omega)$, and in the real space,

$$E(\boldsymbol{r},t)=\frac{1}{(2\pi)^4}\iint d\boldsymbol{q}d\omega[E(\boldsymbol{q},\omega)e^{-i\omega t-i\boldsymbol{q}\cdot\boldsymbol{r}}+E(-\boldsymbol{q},-\omega)e^{i\omega t+i\boldsymbol{q}\cdot\boldsymbol{r}}] \tag{S19}$$

Here only the photon wave vector $\boldsymbol{k}$ is present (i.e., $E(q)=E(k)\delta(q-k)$), so the dc current conductivity can be simplified as,

$$\xi^{(1)}_{ijk}(\boldsymbol{k},\omega;-\boldsymbol{k},-\omega)=k_l\eta_{ijkl}(\omega,-\omega)-k_l\eta_{jikl}(-\omega,\omega) \tag{S20}$$

In real space,

$$\begin{aligned}j_k^{(dc,(1))}(\boldsymbol{r},t)=\int&\frac{d\boldsymbol{k}d\omega d(-\boldsymbol{k})d(-\omega)}{(2\pi)^8}e^{-i(\omega-\omega)t}e^{i(\boldsymbol{k}-\boldsymbol{k})\cdot\boldsymbol{r}}\\&\cdot\xi^{(1)}_{ijk}(\boldsymbol{k},\omega;-\boldsymbol{k},-\omega)E_i(\boldsymbol{k},\omega)E_j(\boldsymbol{k},-\omega)\end{aligned} \tag{S21}$$

The direction and amplitude of a photon drag current are determined by the incidence angle and wavelength of the beam.

(3) **Orbital photogalvanic effect (OPGE)**

Electric field of a light beam with a polarization of $(\hat{\boldsymbol{x}}+i\sigma\hat{\boldsymbol{y}})$ (σ is the light helicity), and OAM m can be written as,

$$\begin{aligned}\boldsymbol{\mathcal{E}}&=u(\rho,z)(\hat{\boldsymbol{x}}+i\sigma\hat{\boldsymbol{y}})e^{im\phi}\\&=u(\rho,z)((\cos(\phi)+i\sigma\sin(\rho))\hat{\boldsymbol{\rho}}+(-\sin(\phi)+i\sigma\cos(\phi))\hat{\boldsymbol{\phi}})e^{im\phi}\end{aligned} \tag{S22}$$

where right (left) circularly polarized light has $\sigma=1(-1)$, and $|u(\rho,z)|^2$ is the intensity profile. As indicated by Eqn. S22, the beam carrying OAM has a phase distribution in the $\hat{\boldsymbol{\phi}}$ direction, or equivalently, it can be described as having an (equivalent, since it is not well defined in many contexts) azimuthal momentum $q_\phi\hat{\boldsymbol{\phi}}$ besides the wave vector $\boldsymbol{k}$.

Then, the dc current generated by q_ϕ is,

$$\begin{aligned}j_k^{(dc,(1))}(\boldsymbol{r},t)=\int&\frac{d\boldsymbol{q}d\omega d(-\boldsymbol{q})d(-\omega)}{(2\pi)^8}e^{-i(\omega-\omega)t}e^{i(\boldsymbol{q}-\boldsymbol{q})\cdot\boldsymbol{r}}\\&\cdot\xi^{(1)}_{ijk}(\boldsymbol{q},\omega;-\boldsymbol{q},-\omega)E_i(\boldsymbol{q},\omega)E_j(-\boldsymbol{q},-\omega)\end{aligned} \tag{S23}$$

The second order conductivity as a function of ω and $\boldsymbol{q}$ can then be written as,

$$\begin{aligned} \xi^{(1)}_{ijk}(\boldsymbol{q},\omega;-\boldsymbol{q},-\omega) &= q_l\eta_{ijkl}(\omega,-\omega) - q_l\eta_{jikl}(-\omega,\omega) \\ &= iq_l\beta_{ijkl}(\omega,-\omega) \end{aligned} \tag{S24}$$

with $\beta_{ijkl}(\omega,-\omega) = i(-\eta_{ijkl}(\omega,-\omega)+\eta_{jikl}(-\omega,\omega))$ being purely real, and $\beta_{ijkl}(\omega,-\omega) = -\beta_{jikl}(-\omega,\omega)$. To avoid complexities in the cylindrical coordinate Fourier transformation, $j_k^{(dc,(1))}(\boldsymbol{r})$, can be re-expressed as a function of the electric field and its spatial gradients,

$$\begin{aligned} j_k^{(dc,(1))}(\boldsymbol{r}) &= \beta_{ijkl}\int\frac{d\boldsymbol{q}}{(2\pi)^3}iq_lE_i(\boldsymbol{q})\int\frac{d(-\boldsymbol{q})}{(2\pi)^3}E_j(-\boldsymbol{q}) \\ &= \beta_{ijkl}\frac{\partial E_i(\boldsymbol{r})}{\partial x_l}E_j(\boldsymbol{r}) \\ &= \beta_{ijkl}\frac{1}{2}[\frac{\partial E_i(\boldsymbol{r},\omega)}{\partial x_l}E_j(\boldsymbol{r},-\omega) - \frac{\partial E_j(\boldsymbol{r},-\omega)}{\partial x_l}E_i(\boldsymbol{r},\omega)] \end{aligned} \tag{S25}$$

For a LG mode described above, $\boldsymbol{q} = q_\phi\hat{\boldsymbol{\phi}}$, the OPGE current would be,

$$\begin{bmatrix} \mathrm{j}\rho \\ \mathrm{j}\phi \end{bmatrix} = \beta : \begin{bmatrix} 0 & \frac{1}{\rho}\frac{\partial E_\rho}{\partial\phi} - \frac{E_\phi}{\rho} \\ 0 & \frac{1}{\rho}\frac{\partial E_\phi}{\partial\phi} + \frac{E_\rho}{\rho} \end{bmatrix} \otimes \begin{bmatrix} E_\rho \\ E_\phi \end{bmatrix} \propto \frac{m}{\rho}|u(\rho,z)^2| \tag{S26}$$

Phenomenological, this process can be interpreted as a direct angular momentum transfer from photon to electron. Considering a LG beam propagating along $\hat{z}$, the linear momenta associated with this electromagnetic field would be *(4)*,

$$p_\phi \sim \frac{m}{\rho}|u|^2, k_z \sim k|u|^2 \tag{S27}$$

These two terms, p_ϕ and k_z, correspond to the orbital photogalvanic effect (OPGE), and the photon drag effect, respectively. The ratio between the azimuthal momentum p_ϕ related to OAM, and the momentum k_z along $\boldsymbol{z}$ is then,

$$\frac{p_\phi}{k_z} = \frac{m}{k\rho} \tag{S28}$$

A rough estimation for the amplitude of OPGE current can be made, in comparison with photon drag effect: For a light beam with wavelength 1 μm, focused to a spot size of a few μm, p_ϕ and $k_z = \frac{2\pi}{\lambda}$ are of the same order of magnitude. Therefore, it implies that these two currents should have comparable magnitudes. Critically, the OPGE photocurrent is proportional to the OAM number m, as long as the small $\boldsymbol{q}$ condition is satisfied.

Furthermore, analogous to CPGE, the OPGE tensor can be separated into symmetric and anti-symmetric parts (with respect of $i \Leftrightarrow j$, or $\omega \Leftrightarrow -\omega$), and we denote the symmetric part as the linear orbital photogalvanic effect (l-OPGE), which is sensitive to the linear polarization of light; and the antisymmetric part as the circular orbital photogalvanic effect (c-OPGE), which switches upon the change of circular polarization of light,

$$\beta^{-}_{ijkl}(\omega,-\omega) = [\beta_{ijkl}(\omega,-\omega) - \beta_{ijkl}(-\omega,\omega)]/2 \tag{S29}$$

and

$$\beta^{+}_{ijkl}(\omega,-\omega) = [\beta_{ijkl}(\omega,-\omega) + \beta_{ijkl}(-\omega,\omega)]/2 \tag{S30}$$

The c-OPGE and l-OPGE currents are given by,

$$J_k^{(c-OPGE)} = \beta^{-}_{ijkl}\left[E_i(\boldsymbol{r},\omega)\frac{\partial E_j(\boldsymbol{r},-\omega)}{\partial x_l} - E_i(\boldsymbol{r},-\omega)\frac{\partial E_j(\boldsymbol{r},\omega)}{\partial x_l}\right] \tag{S31}$$

$$J_k^{(l-OPGE)} = \beta^{+}_{ijkl}\left[E_i(\boldsymbol{r},\omega)\frac{\partial E_j(\boldsymbol{r},-\omega)}{\partial x_l} + E_i(\boldsymbol{r},-\omega)\frac{\partial E_j(\boldsymbol{r},\omega)}{\partial x_l}\right] \tag{S32}$$

(4) **Implication of OPGE: A direct probe of the topological winding number of light**

As derived by Shintani et al.*(13)*, recalling the expression of the winding number of a 2D vector field $\vec{\boldsymbol{n}} = (n_x, n_y)$ represented by $w_v[n]$,

$$w_v[n] = \frac{1}{2\pi}\oint_C \delta_{ij}\epsilon^{\mu\nu} dx_i \frac{n_\mu}{|\vec{\boldsymbol{n}}|}\frac{\partial}{\partial x_j}(\frac{n_\nu}{|\vec{\boldsymbol{n}}|}) \tag{S33}$$

where $\epsilon^{\mu\nu}$ is the 2D Levi-Civita symbol. The electric field of a OAM beam in the Cartesian coordinate reads,

$$\boldsymbol{E} = u[\cos(m\phi - \omega t)\hat{\boldsymbol{x}} - \sigma\sin(m\phi - \omega t)\hat{\boldsymbol{y}}] \tag{S34}$$

where $u = u(\rho, z)$ is the mode profile (as in Eqn. S22)), m and σ are the OAM and SAM numbers, and ω is its frequency. Then $n_x = u\cos(m\phi - \omega t)$, and $n_y = u\sigma\sin(m\phi - \omega t)$. By inserting Eqn. S34 into Eqn. S33, we can obtain,

$$\begin{aligned} w_v[n] &= \frac{1}{2\pi u^2}\oint_C dxu^2\cos(m\phi-\omega t)(-\sigma\cos(m\phi-\omega t))(\frac{\partial\phi}{\partial x}+\frac{\partial\phi}{\partial y})\cdot m \\ &- dxu^2(-\sigma\sin(m\phi-\omega t)(-\sin(m\phi-\omega t))(\frac{\partial\phi}{\partial x}+\frac{\partial\phi}{\partial y})\cdot m \\ &= -\frac{1}{2\pi}\oint m\cdot\sigma d\phi \\ &= -m\cdot\sigma \end{aligned} \tag{S35}$$

On the other hand, in the $\hat{\boldsymbol{\rho}}$ and $\hat{\boldsymbol{\phi}}$ directions, the c-OPGE currents are given by conductivity tensor elements $\beta^{-}_{\rho\phi\rho\phi}$ and $\beta^{-}_{\rho\phi\phi\phi}$, respectively, and their amplitudes are both proportional to the SAM number (helicity) σ and OAM number m.

Therefore, the OPGE current is a direct probe of the topological winding number of light.

1.4 The photogalvanic effect and symmetry selection rules in $\mathrm{WTe_2}$

Our material system, $\mathrm{WTe_2}$, is a room temperature Weyl semimetal with broken inversion symmetry *(20)*. It belongs to the $\mathrm{C_{2v}}$ point group and $\mathrm{Pmn2_1}$ space group, and can be mechanically exfoliated perpendicular to its c axis (principal axis). The circular photogalvanic effect (CPGE), i.e., under homogeneous optical excitation, is described by,

$$\vec{J}_i = \alpha_{ijk}(E_j(\omega)E_k(-\omega) - E_j(-\omega)E_k(\omega)) \tag{S36}$$

In the Cartesian xyz coordinate system (corresponding to abc crystal axes), the nonzero components in the conductivity tensor α are $\alpha_{xxz} = \alpha_{xzx}, \alpha_{yyz} = \alpha_{yzy}, \alpha_{zxx}, \alpha_{zyy}, \alpha_{zzz}$. Since the α_{xxy} or α_{yxy} elements are not present, only when light polarization has an out of plane component, or equivalently when light is obliquely incident onto the xy plane of $\mathrm{WTe_2}$, it can induce an in-plane CPGE current. Similarly, the linear photogalvanic effect (LPGE) current is described by,

$$\vec{J}_i = \alpha_{ijk}(E_j(\omega)E_k(-\omega) + E_j(-\omega)E_k(\omega)) \tag{S37}$$

The conductivity tensor elements α_{xxx}, α_{yyy}, α_{xxy}, α_{yxy}, α_{xyx} and α_{yyx} are all forbidden by symmetry in $\mathrm{WTe_2}$. Therefore, under normal incidence (onto xy plane), LPGE current also vanishes. On the other hand, the photon drag currents (both LPGE and CPGE parts, discussed in section 3 in detail) are governed by fourth order conductivity tensors. Upon normal incidence (light propagates along the $\boldsymbol{z}$ direction or crystallographic c axis), the photon momentum is $\boldsymbol{k} = k_z\hat{\boldsymbol{z}}$ (out-of-plane), which does not break the existing 2-fold rotation or mirror symmetries and would leave the effective point group of $\mathrm{WTe_2}$ unchanged. Therefore, under normal incidence, the photon drag effect is also forbidden in our measurements. We note that the radial photon momentum originating from the finite radius of curvature of the optical wavefront is also present in Gaussian and LG beams, and may cause a 'radial photon drag' response when the beam is out of focus, but in all our measurements, the sample plane is close to the focal plane, and this contribution is not likely measurable.

On the other hand, under normal incidence, the s-PGE and OPGE (both l-OPGE and c-OPGE) effects are symmetry allowed, for OAM-carring beams described by Eqn. S22, under normal incidence due to the effective symmetry reductions related to their in-plane spatial dispersion. Also, the thermal current caused by the asymmetric illumination on electrodes is also present, although it does not have any polarization dependence. The characteristics of all possible sources of currents are summarized in Table. S1.

Overall, the photogalvanic effect is forbidden under normal incidence onto $\mathrm{WTe_2}$ flakes unless there exists external symmetry breaking (i.e., from in-plane photon momentum). In section 2, the comparisons between different electrode geometries for collecting OPGE current and some of its characteristics will be discussed. In section 3, we will analyze other possible external contributions that may lead to symmetry reductions, and experiments to rule out these possibilities.

	Thermal current	PGE	Photon drag	s-PGE	Scattering effects	OPGE
Allowed under normal incidence	Yes	No, unless crystal has external symmetry breaking	No, unless crystal has external symmetry breaking	Yes	Yes	Yes
Direction	Along thermal gradients	/	/	azimuthal and radial	random	azimuthal and radial
Dependence on linear polarization	No	/	/	Yes	Possible	Yes
Dependence on circular polarization	No	/	/	Yes	Possible	Yes
Dependence on OAM index m	Through intensity distribution	/	/	Yes, through intensity distribution	No	Yes, proportional to m
Difference between OAM +m and -m	No	/	/	No	No	Yes, ooposite

Table S1: A comparison between various possible photocurrent sources.

2 Supporting data and analysis

2.1 Experimental designs for collecting azimuthal and radial currents

Unlike the widely studied photogalvanic effect under the plane-wave approximation where the photocurrent flows in a certain direction determined by the conductivity tensor elements, the photocurrent from a OAM-carrying beam may change direction with spatial position, i.e, in the radial/ azimuthal directions. Therefore, the collection of such kind of current needs special experimental designs.

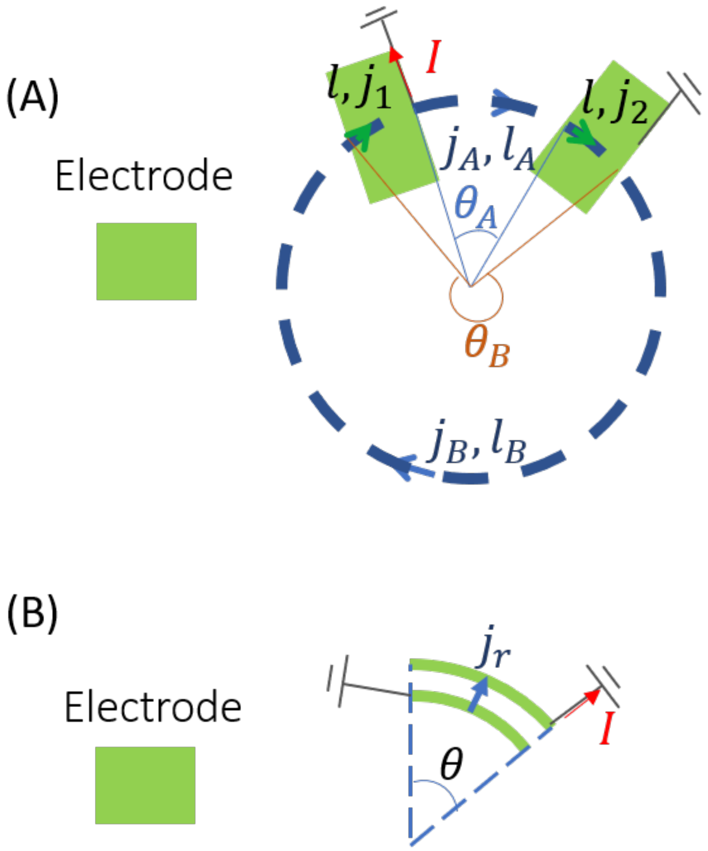

Figure S3: Electrode geometry arrangements for detecting (A) azimuthal and (B) radial photocurrents.

1. Azimuthal current

Here we explain via a simple electrostatic model how an orbiting current could be measured in our experiments (Fig. S3a). The electrons flowing out from the two electrodes are at the same chemical potential (grounded). For the ring geometry shown, A (B) stands for the shorter, length l_A (longer, length l_B) segment of the circle, j_A (j_B) is the current magnitude flowing in the shorter (longer) segments of the loop, respectively. j_1 and j_2 are the currents flowing inside the electrodes. Assuming that both electrodes have length l and the conductivity is σ in the system. $j_s = \sigma \boldsymbol{F}/e$ would be the azimuthal current generated upon light illumination, where $\boldsymbol{F}$ is the effective force on electrons. The measured current is $I = j_A - j_B$. At equilibrium,

$$\begin{aligned} &\frac{1}{\sigma}(j_A l_A + j_2 l) = 0; \\ &\frac{1}{\sigma}(j_B l_B + j_1 l) = 0 \end{aligned} \tag{S38}$$

and

$$\begin{aligned} j_A &= j_2 - j_s; \\ j_B &= j_1 - j_s; \end{aligned} \tag{S39}$$

which can be solved to obtain $I = j_A - j_B = j_s \cdot \frac{l(l_A - l_B)}{(l_A + l)(l_B + l)}$. This is for the case where only current generated at a single radius is collected, but in reality, the electrodes span finite lengths in the radial direction, and the measured current J would be a radial integral of I(r). $J = \int_{r_1}^{r_2} I(r)dr$ where r_1 and r_2 are the radius of the two ends of an electrode, respectively. From the phenomenological model, local OPGE current $j(r,\phi) \propto (\nabla_\phi E)E \propto m\frac{1}{r}|E(r,\phi)|^2$, hence $J \propto m\int_{r_1}^{r_2} \frac{1}{r}|E|^2 \frac{l(r\theta_A - r\theta_B)}{(r\theta_A + l)(r\theta_B + l)}dr$, where θ_A and θ_B are the azimuthal angles formed by two arcs, l_A and l_B, respectively. Therefore, for each LG mode, the OPGE current is proportional to a geometrical factor determined by the electrodes. On the other hand, the measured s-PGE current from beam intensity gradient as an integral of the local s-PGE current, can be written as $J_{s-PGE} \propto \int_{r_1}^{r_2} \frac{\partial |E(r)|^2}{\partial r} \frac{l(r\theta_A - r\theta_B)}{(r\theta_A + l)(r\theta_B + l)}dr$ when the beam is at the center of the arc formed by electrodes.

2. Radial current

As shown in Fig. S3b, between a pair of concentric arcs with a subtended angle θ, an electrical potential would build up due to the radial photocurrent j_r (or the associated electromotive force). Collected I is an integral of $j_r(\phi)|_0^\theta$. The integral from r_1 to r_2 would be $I \propto \int_0^\theta \int_{r_1}^{r_2} j_r(\phi) r dr d\phi$. Since from the phenomenological model, local OPGE current $j_r(\phi) \propto \nabla_\phi E E \propto m\frac{1}{r}|E|^2$, $J_{OPGE} \propto m\int_{r_1}^{r_2} |E|^2 dr$. Again, for each LG mode, there is a geometrical factor determined by the electrode geometry and beam parameters. Similarly, s-PGE current integral is given by $J_{s-PGE} \propto \int_{r_1}^{r_2} \frac{\partial |E|^2}{\partial r} r dr$.

2.2 Photocurrent data from various electrode geometries

A critical aspect of this study is to design suitable electrodes for measuring and identifying photocurrents from helical phase of light. Below we will discuss several electrode geometries and the photocurrent data from OAM beams. Specifically, the photocurrent data from OAM +4 and -4 beams with a same intensity profile but opposite helical phase distributions were plotted and compared, and the similarities and differences between various electrode geometries were examined. Especially, as discussed in detail below, these results provide an evidence of the nonlocality of OPGE current, that is, its direction and amplitude vary in space.

1. ’U’ shaped electrode geometry

A ’U’ shaped electrode pair is made of two concentric semicircles and two parallel arms, which enables a $\sim 180^\circ$ solid angle collection of radial current when the center of the beam is placed at the center of the electrode semicircles. Photocurrents from OAM beams measured using this geometry has been discussed in detail in the main paper (Fig. 2).

2. ’Angular bracket’ shaped electrode geometry

Since the OPGE current flows in the radial direction, as long as the two electrodes are concentric, the subtended angle should be changeable. Here we show an example: While the ’U’ shaped electrodes capture photocurrent in a $\theta = 180^\circ$ solid angle, ’Angular bracket’ shaped electrodes (Fig. S4a, b) collect an integral of current within a $\theta \sim 90^\circ$ solid angle. The green arrows represent the hypothetical OPGE current flowing directions. Considering the C_{2v} symmetry of the material platform, $\mathrm{WTe_2}$, the conductivity coefficients along the crystal a and b axes are unequal, and the direction of the net current collected by the two electrodes would depend on tensor elements both associated with q_x, and q_y, which varies with the alignment of the electrodes with respect to the crystal axes. Despite its geometry difference from the ’U’ shape, the OPGE phenomena were again observed (Fig. S4c, d), i.e., $\frac{1}{2}(\mathrm{J_{LCP}} - \mathrm{J_{RCP}})$ adopt different signs for OAM +4 and -4 beams. Therefore, it provides further evidence of the existence of the radial OPGE current.

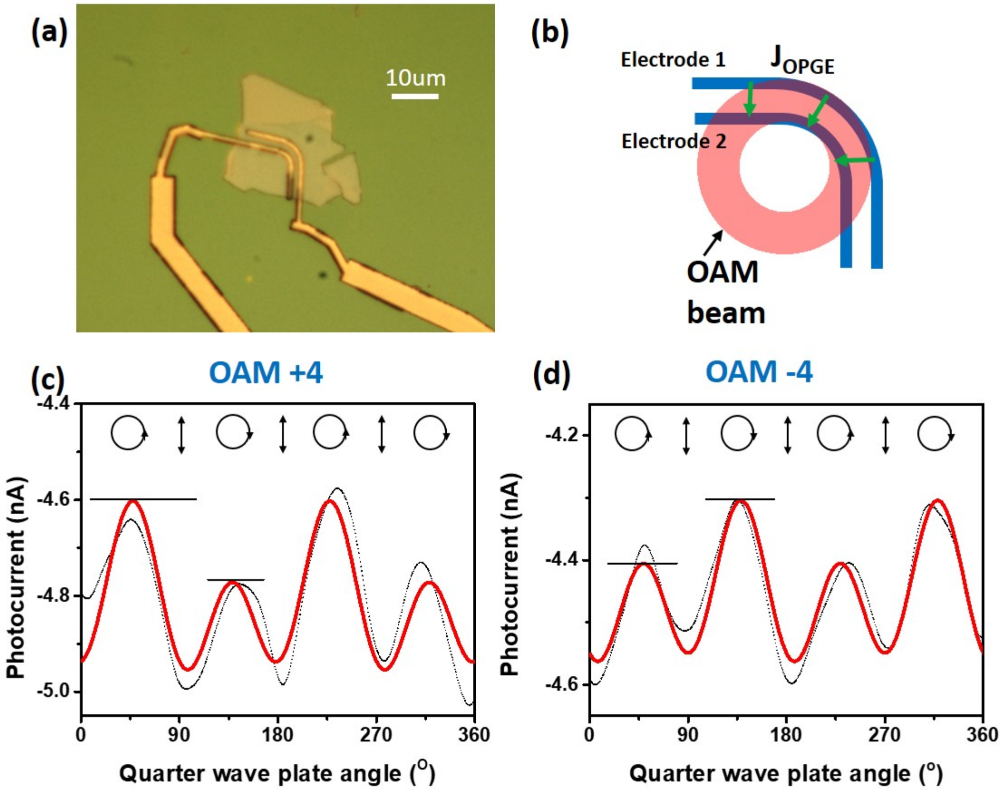

Figure S4: Photocurrent measurement using 'angular bracket' shaped electrodes. (a) Optical image of the device on an exfoliated single-crystalline $\mathrm{WTe_2}$ flake. Scale bar: 10 $\mu\mathrm{m}$. (b) Schematic of the photocurrent collection. (c, d) Photocurrent data from (c) OAM +4 and (d) OAM -4 beam.

3. ’Ω’ shaped electrode geometry

Since the existence of s-CPGE may sometimes increase the complexity of OPGE current measurement, we designed the $'\Omega'$ shaped electrodes to avoid this problem. As shown in Fig. S5a, these electrodes forming an $'\Omega'$ shape were designed to collect the azimuthal part of the OPGE current. When the beam center is at the center of the arcs, and its ring distance ($\rho_0 = \sqrt{\frac{|m|}{2}} w_0$) coincides with the radius of the electrodes (Fig. S5a, b), there will be maximized intensity, but vanishing intensity gradient along the circumference defined by the electrodes, which means that the contribution from the s-CPGE is effectively eliminated, and the collected helicity dependent photocurrent would be from OPGE. The photocurrent data is plotted in Fig. S5c, d, once again showing the sensitivity of OPGE current to light helicity, and its sign reversal upon light incidence with opposite OAM numbers. This measurement provides evidence of the presence of azimuthal OPGE current.

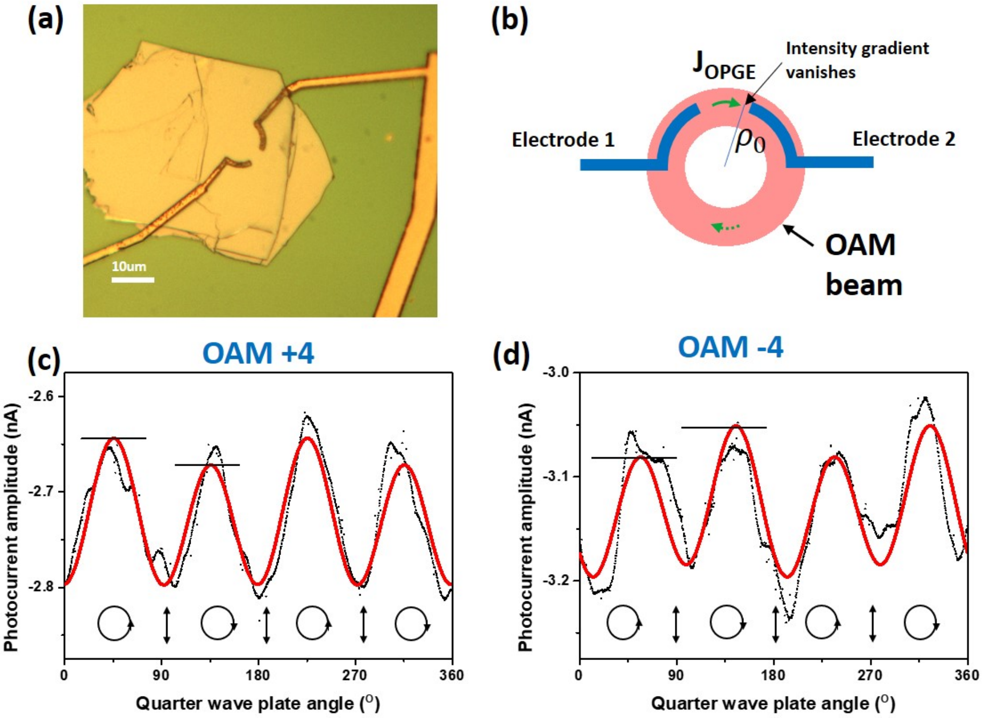

Figure S5: Photocurrent measurement using ’Ω’ shaped electrodes. (a) An optical image of the device (b) A schematic of the photocurrent measurement. The ring distance of the LG beam coincides with the radius of the electrodes (c, d) Photocurrent data from OAM +4 and OAM -4 beams.

4. ’Starfish’ shaped electrode geometry

In a ’Starfish’ electrode geometry, photocurrent could be measured between each of the nearest electrode pairs (i.e., from A to B, B to C, C to D and D to E electrodes). Since the electrodes span some length in the radial direction, the collected photocurrent is a space integral of $J_{OPGE}(\rho, \phi)$. Fig. S6 shows the electrode geometry and data from one of such devices. OAM +4, OAM -4 beams were measured, and the OPGE voltage signal between nearest electrode pairs always have opposite signs. Also, for OAM +4 (blue color), the OPGE current was always flowing clockwise, while for OAM -4 (green color), its OPGE current was flowing counterclockwise. This is a further evidence that OPGE current flows in the azimuthal direction.

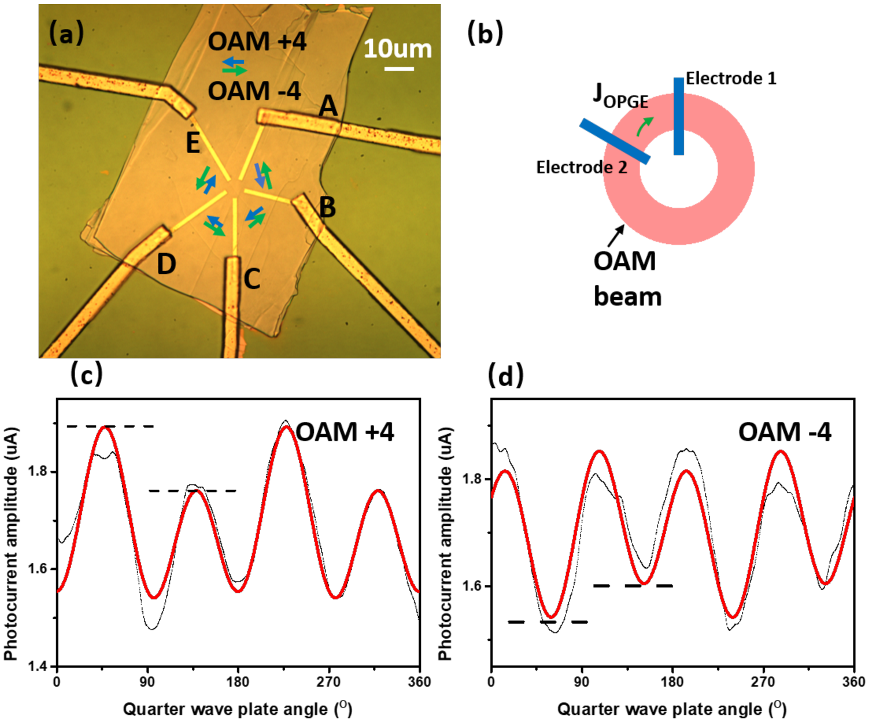

Figure S6: Photocurrent measurement using ’Starfish’ shaped electrodes. (a) The arrows indicate the sign of OPGE voltage between the nearest electrode pairs. Blue and green colors represent OAM +4 and OAM -4, respectively. (b) A schematic of the azimuthal photocurrent measurement using ’Starfish’ shaped electrodes. (c, d) Photocurrent data between A and B electrodes, from OAM (c) +4 and (d) -4 beams.

2.3 Spatial and beam size dependence of OPGE current

In order to find the characteristics of OPGE current, with the U-shaped electrode geometry (for collecting radial current), the spot size and spatial dependence of OPGE current were measured, using OAM +4 and -4 beams. From S1.3, S1.4, if the current response depending on circular polarization is measured, and by comparing OAM number +m and -m responses, i.e., $(J_{C,+m} - J_{C,-m})/2$, where J_C is the part of measured photocurrent that switches upon circular polarization, then the OPGE current response is unambiguously determined.

(1) Spatial dependence

The spatial dependence of OPGE current along $\boldsymbol{x}$ direction is shown in Fig. S7. When the beam center is at the center of the arcs (formed by two electrodes), i.e. at spot S4, the current magnitude reaches its maximum; and as the beam center moves away from the center, either to the left or to the right, the OPGE current magnitude gradually decreases.

The spatial dependence along $\boldsymbol{y}$ is shown in Fig. S8. It has a similar trend that as spot gets further away from the center of the arcs, OPGE current magnitude decreases. Combining the result in the two perpendicular directions, this is an evidence that *OPGE current is flowing in radial direction*, instead of directions determined by the crystal axes, as in conventional PGE. Also, since the electrode pair offer a good confinement for currents flowing in between, the collected current amplitude is actually proportional to the solid angle formed by the center of the beam, and the electrodes. When the beam is off-centered, the solid angle would decrease.

(2) Beam size dependence

The photocurrent data measured at six different beam sizes (w_0) is shown in Fig. S9 (a), and OPGE current amplitude is plotted as a function of the spot size in Fig. S9 (b), and fitted by the expression of collected OPGE current (introduced in S2.1) as shown as the red curve. As the spot size changes, the OPGE current first increases, reaches its maximum, then decreases. When the current reaches maximum, the beam size is comparable with the half circles of 'U' shaped electrodes.

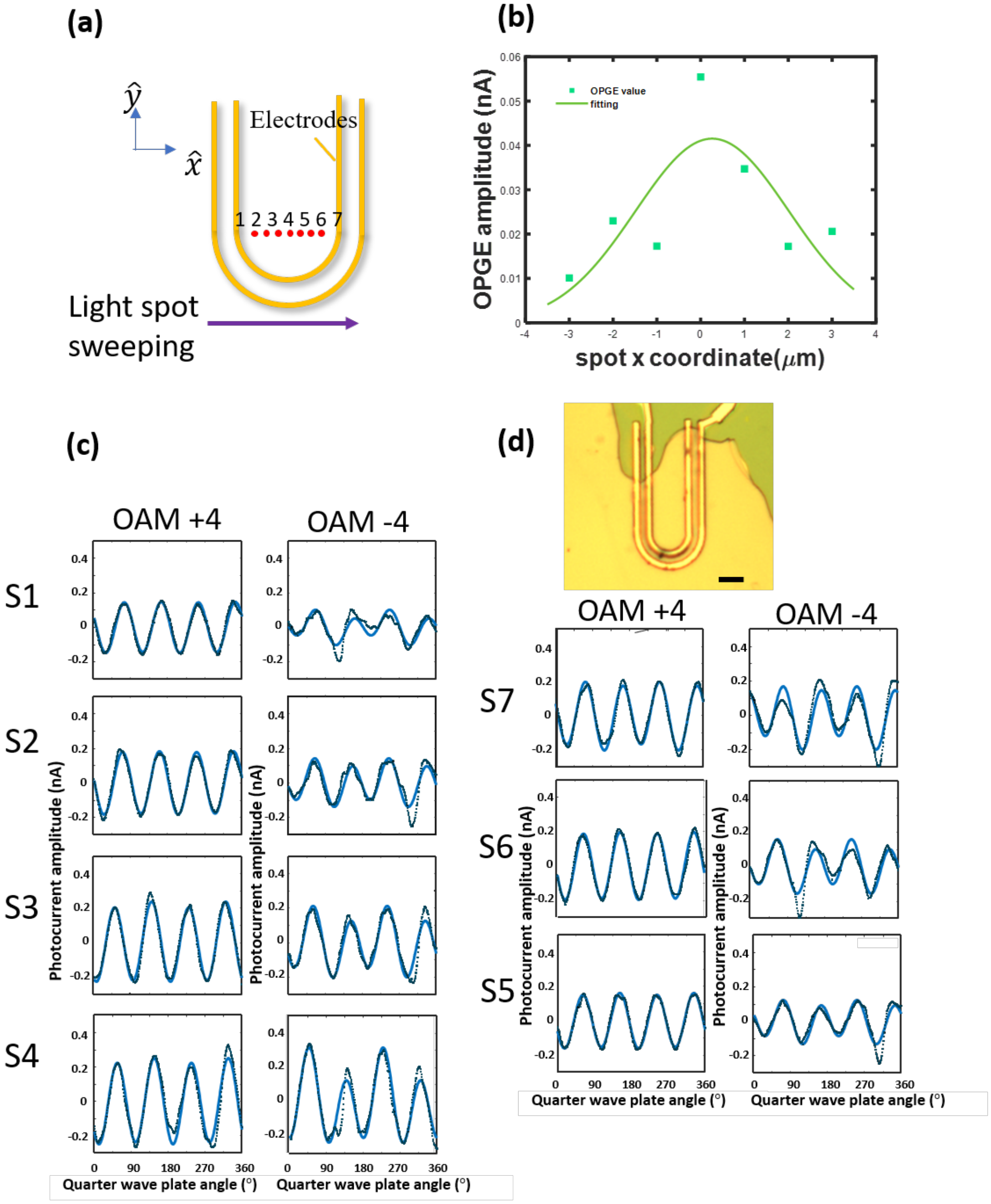

Figure S7: OPGE current measurements using 'U' shaped electrodes from OAM +4 and -4 beams while moving the spot along x direction. (a) Schematic of the 'U' shaped electrodes, and beam center locations are represented by the red dots. (b) The OPGE current magnitude as a function of the x coordinate. (c) Photocurrent data measured at seven locations, from S1-S7. (d) An image of the nanodevice, scale bar: 10 um.

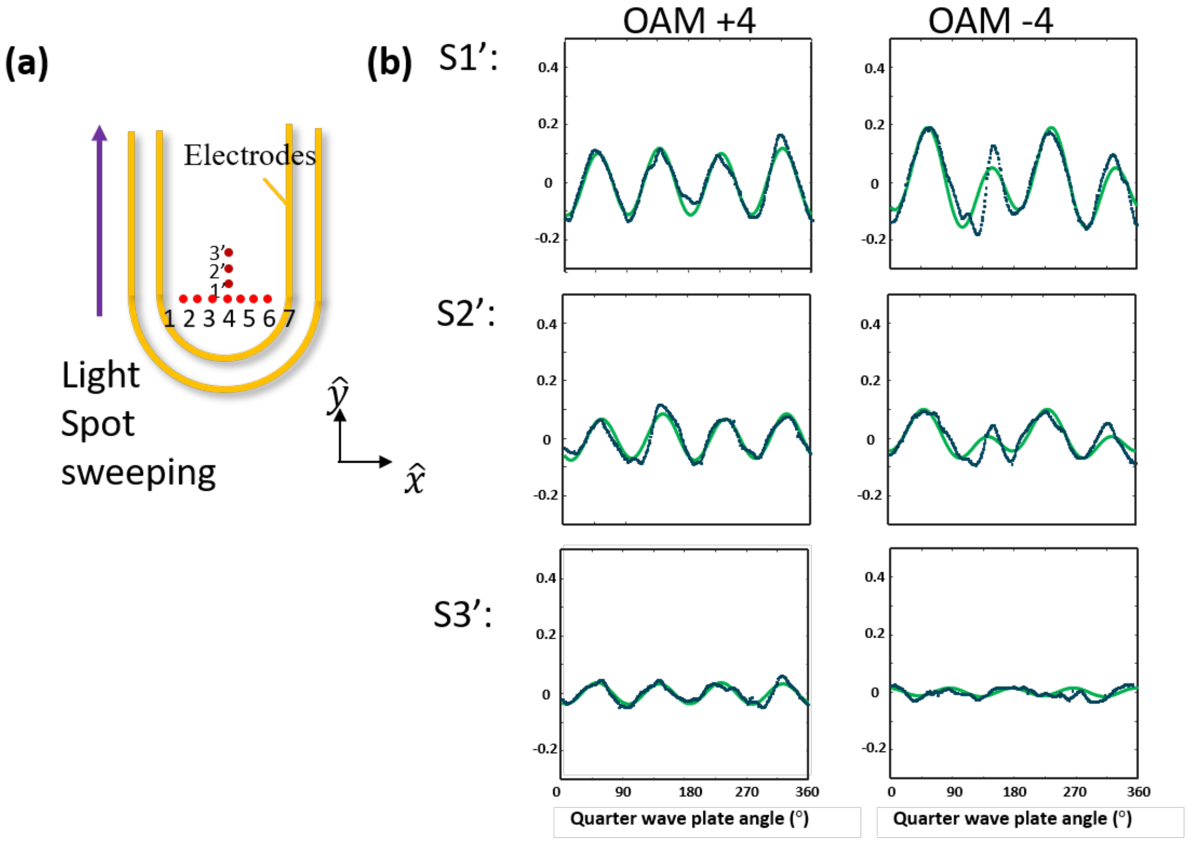

Figure S8: OPGE current measurements using 'U' shaped electrodes from OAM +4 and -4 beams while moving the spot along y direction. (a) Schematic of the 'U' shaped electrodes, where beam center locations are represented by the dark red dots (b) Original data measured at three locations, from S1'-S3'.

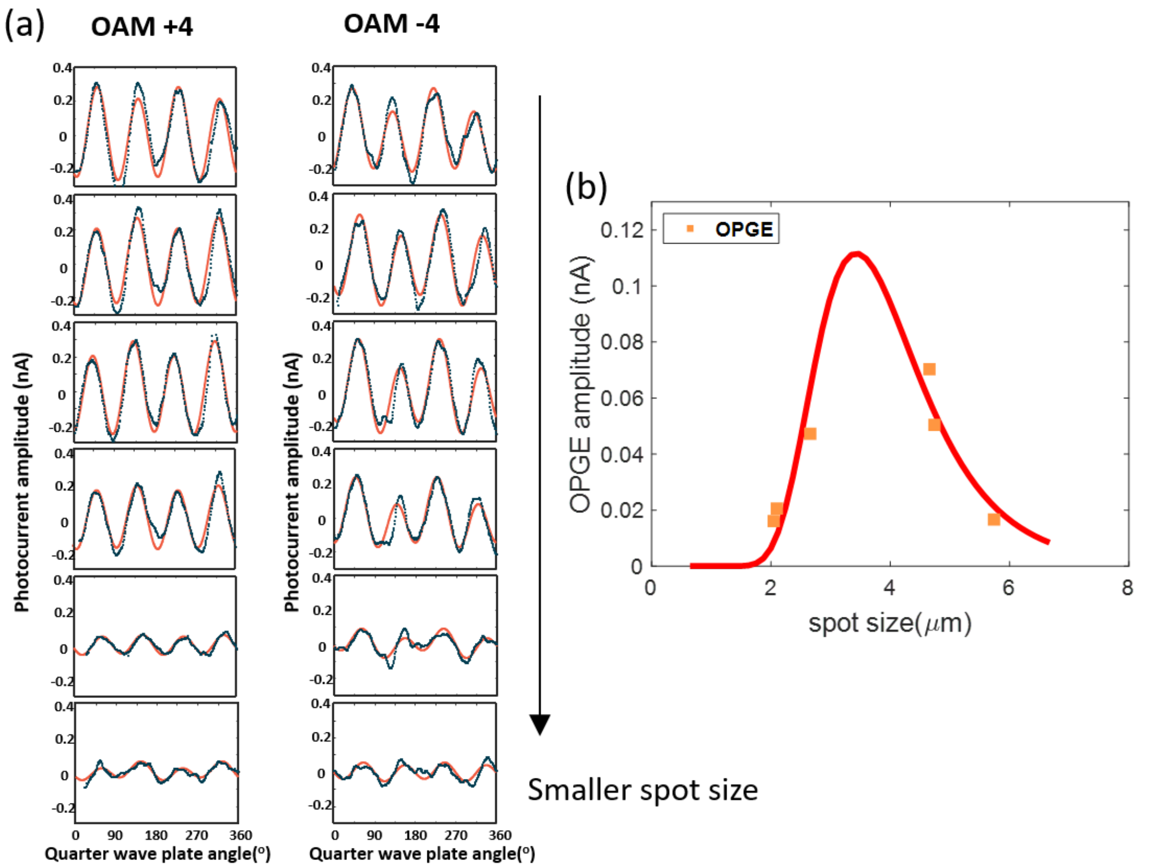

Figure S9: Spot size dependence of OPGE current measured using ’U’ shaped electrodes from OAM +4 and -4 beams. (a) Original photocurrent data measured at six different spot sizes. (b) The OPGE current magnitude as a function of the spot size (orange squares) and fitting result (red curve).

2.4 'Discretized' OPGE current

To further discuss the results from the 'discretized' OPGE current measurement, the integral parameters of OPGE current were calculated for different LG beams ($m = 1, 2, 3, 4$).

Azimuthal geometry ('starfish' shaped electrodes) As described in section 2.1, based on

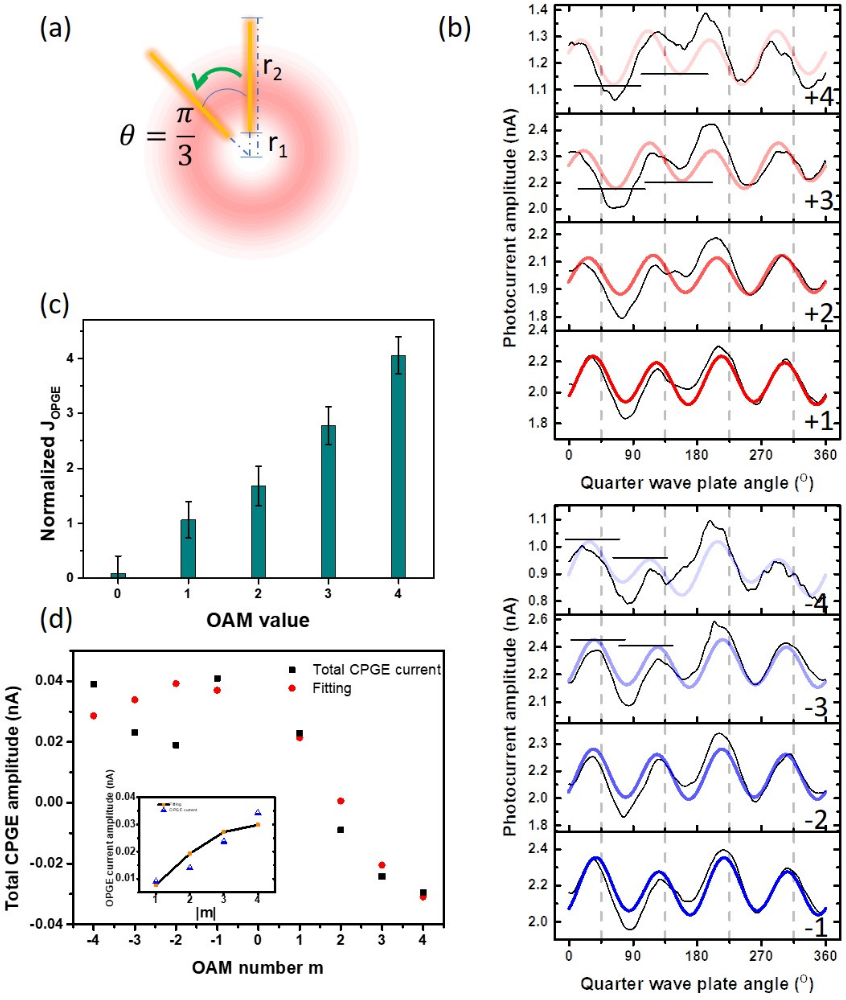

Figure S10: (a) A simple model for the azimuthal photocurrent collection. (b) Original photocurrent data as a function of the quarter wave plate angle, collected by the 'starfish' shaped electrodes, from OAM -4 to 4 beams. (c) Extracted OPGE current, $J_{OPGE} = \frac{J_{C,m} - J_{C,-m}}{2}$. (d) The comparison between fitting (red dots) and experimental data (black dots) of $J_C = J_{OPGE} + J_{s-CPGE}$. (Inset) The corresponding fitting and experimental data of J_{OPGE}.

the electrostatic model, the two equations used for calculating collected azimuthal photocurrent are $J_{OPGE} \propto m \cdot \int_{r_1}^{r_2} \frac{1}{r}|E|^2 \frac{l(r\theta_A - r\theta_B)}{(r\theta_A + l)(r\theta_B + l)} dr = c \cdot m$ with c being the geometrical constant dependent on LG mode profiles, and $J_{s-PGE} \propto \int_{r_1}^{r_2} \frac{\partial |E|^2}{\partial r} \frac{l(r\theta_A - r\theta_B)}{(r\theta_A + l)(r\theta_B + l)} dr$. The known experimental parameters are $\theta_A \sim \frac{\pi}{3}$, $r_2 \sim 5r_1$ (Fig. S6 & S10 (a)). The original photocurrent data as a function of the quarter wave plate angle is shown in Fig. S10 (b), and the extracted OPGE current amplitudes from different LG beams are plotted in Fig. S10 (c). It can be seen that as OAM order increases, the OPGE current becomes larger monotonically, and it has a nearly linear dependence on the OAM index. In Fig. S10 (c), the fitting result (with parameter $\omega_0 = 1.1r_1$) is that the total CPGE is a sum of s-CPGE and OPGE, with two parts of amplitudes being comparable with each other when $m \leq 2$, and OPGE takes up a larger portion when $m \geq 2$. When the photocurrent from different OAM orders are normalized by the geometrical constants c of LG beams, its trend follows the proportionality rule between OAM number and the local OPGE current.

Radial geometry ('U' shaped electrodes) As described in section 2.1, the two phenomenonlogical equations used for calculating collected radial photocurrent are $J_{OPGE} \propto m\int_{r_1}^{r_2} |E|^2 dr$ and $J_{s-PGE} \propto \int_{r_1}^{r_2} \frac{\partial |E|^2}{\partial r} r dr$. The known experimental parameters are radii of the electrodes: $r_1 \sim 15um$ and $r_2 \sim 20um$ (Fig. 2 & S11 (a)), and the parameter $w_0 \sim 15um$ for LG beams. The quarter waveplate angle dependent photocurrent data from from OAM -4 to 4, as presented in main paper Figure 2, is shown in Fig. S11 (b), where J_C (the part of photocurrent switches upon circular polarization) is negative for negative OAM beams, and positive for positive OAM beams, and its amplitude increases monotonically with OAM $|m|$. Although the collected current is not guaranteed to be directly proportional to OAM after the spatial integration (because the local intensity distribution are different for different OAM modes), when the geometrical constant of OPGE current are similar for various LG beams at certain beam radius, this discretization could be observed. In Fig. S11d, J_C is fitted as a sum of s-CPGE and OPGE using the above equations, and the result shows that OPGE current is always dominating, as can be seen from the overall trend of increasing from -4 to 4 OAM numbers. Therefore, the experimental data and the fitting curve are in qualitative agreement.

From the agreements between fittings and experiments, and data from radial and azimuthal electrode geometries, for eight OAM orders, it points to the conclusion that the local OPGE current is proportional to OAM order. Furthermore, since OAM +m and -m beams are related to each other by a mirror operation, when one beam is obtained, it can be routed into two beams that incident onto the detector in two opposite directions. Effectively, the photocurrent difference between OAM +m and -m beams can be measured simultaneously. In this way, OPGE current is distinctly collected, through $J_{OPGE} = \frac{J_m - J_{-m}}{2}$, and the OAM order can be subsequently determined.

Protocol for detecting mixtures of different OAM orders If a beam is a mixture of different OAM orders, then the photocurrent distribution will be dependent on the intensity profile of each beam, and a matrix of electrodes could be designed to distinguish it from a single OAM beam. The calculation based on a mixture of n LG modes $LG_0^1 ... LG_0^n$ with

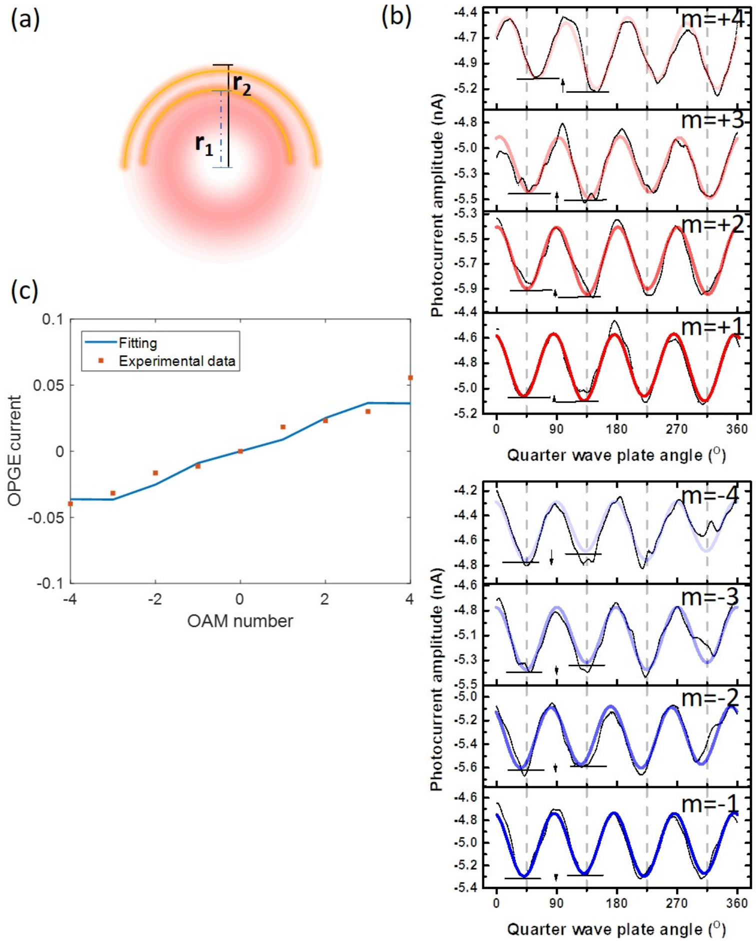

Figure S11: (a) A schematic for the radial photocurrent collection. (b) Original photocurrent data as a function of the quarter wave plate angle, collected by the 'U' shaped electrodes, from OAM -4 to 4 beams. (c) The comparison between fitting (blue curve) and experimental data (red dots) of J_{OPGE}.

percentages $x_1 ... x_n$ reads,

$$\boldsymbol{E}(\rho,\phi)_{mix} = x_1\boldsymbol{E}(LG_0^1) + x_2\boldsymbol{E}(LG_0^2) + ... + x_n\boldsymbol{E}(LG_0^n) \tag{S40}$$

$$J_{OPGE,mix} \propto \frac{e^{-2\rho^2/w_0^2}}{\rho}\left(\frac{x_1}{|1|!}\rho^{|2|} + \frac{2x_2}{|2|!}\rho^{|4|} + ... + \frac{nx_n}{|n|!}\rho^{|2n|}\right) \tag{S41}$$

where ρ is the radial coordinate. For instance, if we have a 50/50 mixture of LG_0^1 mode and LG_0^3 mode, then $J_{1,3} \propto 1/2\rho^2 + 1/4\rho^6$, while for LG_0^2 mode, $J_2 \propto \rho^4$ (prefactor is omitted). It implies that a set of electrodes that collect current at various radial coordinates would be eligible of distinguishing these two cases. An example is shown in Fig. S12. This should work for all complex mixtures of OAM beams. For a beam with a very high OAM order (e.g., >100), the perturbation treatment may needs a modification to include higher order in $\boldsymbol{q}$ terms in Eqn. S13, but in principle, those beams can still be detected.

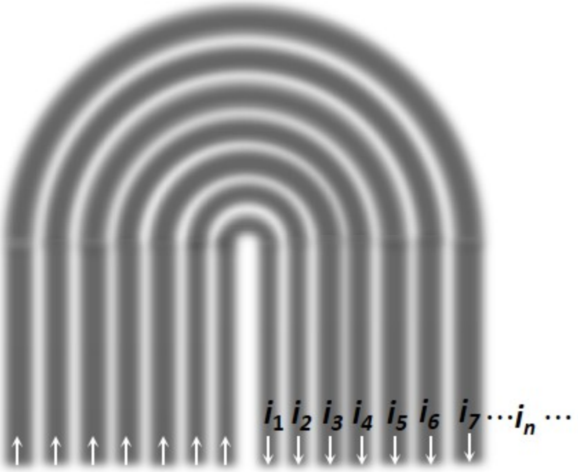

Figure S12: An example of the device geometry for measuring arbitrary mixtures of OAM beams.

2.5 Arbitrary OAM states on the higher order Poincare sphere

An arbitrary state $|\psi\rangle$ on the higher order Poincare sphere (HOPS) can be generated by a q-plate given by,

$$J_{q-plate} = \begin{bmatrix} 0 & ie^{-i2q\phi} \\ ie^{i2q\phi} & 0 \end{bmatrix}$$

combined with a quarter wave plate given by,

$$J_{qwp} = \frac{1}{\sqrt{2}} \begin{bmatrix} 1 & ie^{-i2\alpha} \\ ie^{i2\alpha} & 1 \end{bmatrix}$$

On the HOPS, the optical state $|\psi\rangle$ is then described by *(30)*

$$|\psi\rangle \propto \cos\left(\frac{\Theta}{2}\right) \exp\left(-i\frac{\Phi}{2}\right) |L_{-m}\rangle + \sin\left(\frac{\Theta}{2}\right) \exp\left(i\frac{\Phi}{2}\right) |R_m\rangle \tag{S42}$$

where Θ and Φ are the spherical coordinates on the HOPS, and basis states $|R_m\rangle = \frac{1}{\sqrt{2}}(\hat{\boldsymbol{\rho}} + i\sigma\hat{\boldsymbol{\phi}}) \exp(i(m+\sigma)\phi)$ and $|L_{-m}\rangle = \frac{1}{\sqrt{2}}(\hat{\boldsymbol{\rho}} - i\sigma\hat{\boldsymbol{\phi}}) \exp(-i(m+\sigma)\phi)$ for OAM m, SAM σ HOPS.

According to the expression of OPGE current, with $a_1 = \cos\left(\frac{\Theta}{2}\right) \exp\left(-i\frac{\Phi}{2}\right)$, and $a_2 = \sin\left(\frac{\Theta}{2}\right) \exp\left(i\frac{\Phi}{2}\right)$, and denoting the intensity constant as $|E_0|^2$, then for state $|\psi\rangle$, the OPGE photocurrent along $\boldsymbol{\phi}$ would consists of two parts, $j^{(\phi)}$ and $j^{(0)}$, and below are the derivations:

$$\begin{aligned}
j^{(\phi)}_{OPGE,\phi} &= \gamma_{ijk\phi}(\nabla_\phi E_i E_j^* + \nabla_\phi E_j^* E_i)\\
&= \gamma_{\rho\phi\phi\phi}\{[\frac{\partial E_\rho}{\rho\partial\phi} - \frac{E_\phi}{\rho}]E_\phi^* + [\frac{\partial E_\phi^*}{\rho\partial\phi} + \frac{E_\rho^*}{\rho}]E_\rho\}\\
&+ \gamma_{\phi\rho\phi\phi}\{[\frac{\partial E_\phi}{\rho\partial\phi} + \frac{E_\rho}{\rho}]E_\rho^* + [\frac{\partial E_\rho^*}{\rho\partial\phi} - \frac{E_\phi^*}{\rho}]E_\phi\}\\
&+ \gamma_{\rho\rho\phi\phi}\{[\frac{\partial E_\rho}{\rho\partial\phi} - \frac{E_\phi}{\rho}]E_\rho^* + [\frac{\partial E_\rho^*}{\rho\partial\phi} - \frac{E_\phi^*}{\rho}]E_\rho\}\\
&+ \gamma_{\phi\phi\phi\phi}\{[\frac{\partial E_\phi}{\rho\partial\phi} + \frac{E_\rho}{\rho}]E_\phi^* + [\frac{\partial E_\phi^*}{\rho\partial\phi} + \frac{E_\rho^*}{\rho}]E_\phi\}\\
&= \frac{m}{\rho}|E_0|^2[\sigma(\gamma_{\phi\rho\phi\phi} + \gamma_{\rho\phi\phi\phi})\cos(\Phi + 2(m+\sigma)\phi)\\
&+ (-\gamma_{\rho\rho\rho\rho} + \sigma^2\gamma_{\phi\phi\phi\phi})\sin(\Phi + 2(m+\sigma)\phi)]\sin\Theta
\end{aligned}\tag{S43}$$

Besides, the part not varying with azimuthal angle reads,

$$\begin{aligned}
j^{(0)}_{OPGE,\phi} &= \beta_{ijk\phi}(\nabla_\phi E_i E_j^* - \nabla_\phi E_j^* E_i)\\
&= \beta_{\rho\phi\phi\phi}\{[\frac{\partial E_\rho}{\rho\partial\phi} - \frac{E_\phi}{\rho}]E_\phi^* - [\frac{\partial E_\phi^*}{\rho\partial\phi} + \frac{E_\rho^*}{\rho}]E_\rho\}\\
&+ \beta_{\phi\rho\phi\phi}\{[\frac{\partial E_\phi}{\rho\partial\phi} + \frac{E_\rho}{\rho}]E_\rho^* - [\frac{\partial E_\rho^*}{\rho\partial\phi} - \frac{E_\phi^*}{\rho}]E_\phi\}\\
&+ \beta_{\rho\rho\phi\phi}\{[\frac{\partial E_\rho}{\rho\partial\phi} - \frac{E_\phi}{\rho}]E_\rho^* - [\frac{\partial E_\rho^*}{\rho\partial\phi} - \frac{E_\phi^*}{\rho}]E_\rho\}\\
&+ \beta_{\phi\phi\phi\phi}\{[\frac{\partial E_\phi}{\rho\partial\phi} + \frac{E_\rho}{\rho}]E_\phi^* - [\frac{\partial E_\phi^*}{\rho\partial\phi} + \frac{E_\rho^*}{\rho}]E_\phi\}\\
&= \frac{m}{\rho}|E_0|^2[\sigma(\beta_{\phi\rho\phi\phi} - \beta_{\rho\phi\phi\phi})\\
&+ (-i\beta_{\rho\rho\rho\rho} - i\sigma^2\beta_{\phi\phi\phi\phi})\cos\Theta]
\end{aligned}\tag{S44}$$

Eqn S43 and S44 correspond to Eqn. 4 in the main text. The $j^{(\phi)}$ term has a period of $\pi/(m+\sigma)$ when varying with azimuthal angle ϕ, while the $j^{(0)}$ terms describe current flowing homogeneously in the $\hat{\phi}$ direction. For some special points:

1. The poles: P1 ($(0,\Phi)$, or $(a_1,a_2) = (1,0)$) and P2 ((π,Φ), or $(a_1,a_2) = (0,1)$), $\sin\Theta = 0$, hence $j^{(\phi)}_{OPGE,\phi}$ vanishes. Especially, the c-OPGE part for these two points is $j^{(0)}_{c-OPGE,\phi} = \frac{m\sigma}{\rho}|E_0|^2(\beta_{\phi\rho\phi\phi} - \beta_{\rho\phi\phi\phi})$, proportional to both the OAM number m and SAM number σ, or the topological winding number of the light beam (as discussed in S1.3) for scalar OAM beams.

2. Radially / azimuthally polarized beam (special points on the equator): For states P3 ($(\pi/2,0)$, or $(a_1,a_2) = (\sqrt{2}/2,\sqrt{2}/2)$) and P4 ($(\pi/2,\pi)$, or $(a_1,a_2) = (-\sqrt{2}i/2,\sqrt{2}i/2)$),

their Φ angles have a π phase shift, so they have equal and opposite $j^{(\phi)}_{OPGE,\phi}$.

If we take a closer look at $j_\phi^{(c-OPGE,(\phi))}$,

$$j_\phi^{(c-OPGE,(\phi))} \propto \frac{m\sigma}{\rho}\sin(\Theta)\cos(2(m+\sigma)\phi+\Phi)) \tag{S45}$$

It implies that the ϕ (spatial) dependence of the OPGE current can be mapped onto Φ coordinates (through the total angular momentum $J = m + \sigma$), and its amplitude is directly related to the Θ coordinate, so that the coordinates on the HOPS can be determined by measuring OPGE currents. (For simplicity, the anisotropies in conductivity coefficients are not considered explicitly. Depending on the crystal symmetries of the material system, their ϕ dependencies may vary).

Next, let's consider the photocurrent at a certain spatial location (ρ, ϕ), from an arbitrary state (Θ, Φ), after transmitting through a quarter/ half wave plate (or with a specific phase retardation). Starting with a state $|\psi\rangle = a_1 |L_{-m}\rangle + a_2 |R_m\rangle$, the transformation of $|L_{-m}\rangle$ under a quarter wave plate at angle α is,

$$\begin{aligned}\left|L'_{-m}\right\rangle = J_{QWP}\left|L_{-m}\right\rangle &= \frac{1}{\sqrt{2}}\begin{bmatrix}1 & ie^{-i2\alpha}\\ ie^{i2\alpha} & 1\end{bmatrix} * \begin{bmatrix}1\\0\end{bmatrix} e^{-im\phi}\\ = \frac{1}{\sqrt{2}}\begin{bmatrix}1\\ ie^{i2\alpha}\end{bmatrix} e^{-im\phi} &= \frac{1}{\sqrt{2}}\left|L_{-m}\right\rangle + \frac{1}{\sqrt{2}} ie^{i2\alpha}\left|R_{-m}\right\rangle\end{aligned} \tag{S46}$$

For $|R_{+m}\rangle$, it is,

$$\begin{aligned}|R'_m\rangle = J_{QWP}|R_m\rangle &= \frac{1}{\sqrt{2}}\begin{bmatrix}1 & ie^{-i2\alpha}\\ ie^{i2\alpha} & 1\end{bmatrix} * \begin{bmatrix}0\\1\end{bmatrix} e^{im\phi}\\ = \frac{1}{\sqrt{2}}\begin{bmatrix}ie^{-i2\alpha}\\ 1\end{bmatrix} e^{im\phi} &= \frac{1}{\sqrt{2}} ie^{-i2\alpha}|L_m\rangle + \frac{1}{\sqrt{2}}|R_m\rangle\end{aligned} \tag{S47}$$

Then, the new state would be

$$|\psi'\rangle = a_1\left|L'_{-m}\right\rangle + a_2|R'_m\rangle \tag{S48}$$

Eqn. S45 can be modified accordingly, and the term with $2\alpha_{qwp}$ dependence reads,

$$j_\phi^{(c-OPGE,(\phi))} \propto \frac{m\sigma}{\rho}\sin(\Theta)\cos(2m\phi+\Phi-2\alpha_{qwp})) \tag{S49}$$

To verify Eqn. S49 experimentally, we define a new OPGE current $\Delta j^{(\phi)}_{OPGE,\phi}$, i.e., $\Delta j^{(\phi)}_{OPGE,\phi} = j^{(\phi)}_{OPGE,\phi}|_{\alpha_{qwp}} - (j^{(\phi)}_{OPGE,\phi}|_{\alpha_{qwp}=\pi/4} + j^{(\phi)}_{OPGE,\phi}|_{\alpha_{qwp}=3\pi/4})/2$, then $j = \Delta j^{(\phi)}_{OPGE,\phi}|_{\pi/4} - \Delta j^{(\phi)}_{OPGE,\phi}|_{3\pi/4}$ has two characteristics: 1. When (Θ, Φ) coordinates are fixed, j measured at $\phi = 0$ and $\phi = \pi/2$ would be opposite. 2. When azimuthal angle ϕ is fixed, then j measured from $(\Theta, \Phi = 0)$ and $(\Theta, \Phi = \pi)$ states would again be opposite. Therefore, in our experiment, we chose P3 $((\pi/2, 0)$ and P4 $((\pi/2, \pi)$ states, measured photocurrent at $\phi = 0$ and

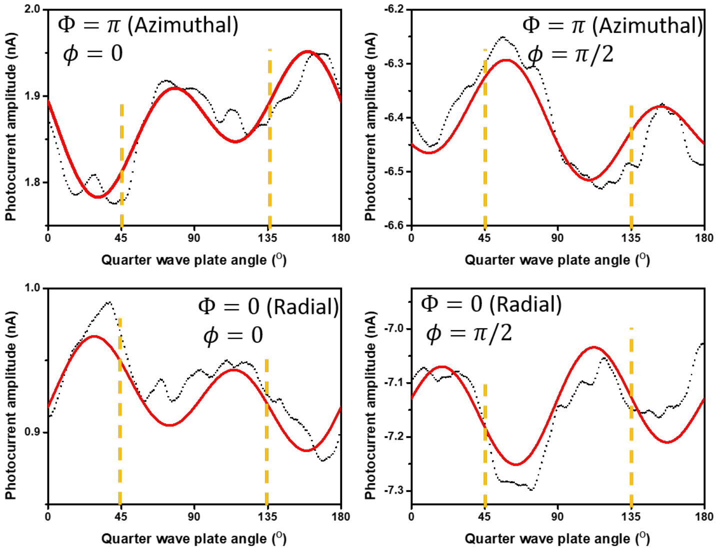

Figure S13: Photocurrent data as a function of the quarter wave plate angle, from states P3 $(\pi/2, 0)$ and P4 $(\pi/2, \pi)$ on the HOPS, measured at two spatial locations, $\phi = 0$ and $\phi = \pi/2$.

$\phi = \pi/2$ azimuthal angles, plotted, and compared the current amplitudes at $\alpha_{qwp} = \pi/4$ and $\alpha_{qwp} = 3\pi/4$. The data collected from a full period of α_{qwp} in $[0, \pi]$, is plotted in Fig. S13.

Meanwhile, $j_{\phi}^{(OPGE,(0))}$ has both a $\cos(\Theta)$ dependence and a $\cos(2\alpha_{qwp} + \alpha_0)$ dependence (note here $\nabla_{\rho}E$, the radial intensity gradient may also contribute), and this characteristic could be used to determine the Θ coordinate. In our measurement, as shown in Fig. 3c in the main text, upon changing the optical state from P1 to P5, from P5 to, P2, Θ changes by π ($\Delta\Theta = \pi$), the photocurrent fitted by $J = J_c \sin(2\alpha_{qwp} + \alpha_1) + J_l \sin(4\alpha_{qwp} + \alpha_2) + J_0$ has a change in J_C from its maximum to its minimum monotonically, confirming the dependence of $j_{OPGE,\phi}$ on the Θ coordinate. The full dependence of photocurrent on α_{qwp} is shown in Fig. S14.

On the other hand, the transformation of $\left|L_{-m}\right\rangle$ under a half wave plate (with angle α) is:

$$\begin{aligned}\left|L'_{-m}\right\rangle &= J_{hwp}\left|L_{-m}\right\rangle = \frac{1}{\sqrt{2}}\begin{bmatrix}0 & ie^{-i2\alpha}\\ ie^{i2\alpha} & 0\end{bmatrix} * \begin{bmatrix}1\\0\end{bmatrix} e^{-im\phi}\\ &= \frac{1}{\sqrt{2}}\begin{bmatrix}0\\ ie^{i2\alpha}\end{bmatrix} e^{-im\phi} = \frac{1}{\sqrt{2}} ie^{i2\alpha}\left|R_{-m}\right\rangle\end{aligned} \tag{S50}$$

For $\left|R_{+m}\right\rangle$, it is:

$$\begin{aligned}\left|R'_{m}\right\rangle &= J_{hwp}\left|R_{m}\right\rangle = \frac{1}{\sqrt{2}}\begin{bmatrix}0 & ie^{-i2\alpha}\\ ie^{i2\alpha} & 0\end{bmatrix} * \begin{bmatrix}0\\1\end{bmatrix} e^{im\phi}\\ &= \frac{1}{\sqrt{2}}\begin{bmatrix}ie^{-i2\alpha}\\ 0\end{bmatrix} e^{im\phi} = \frac{1}{\sqrt{2}} ie^{-i2\alpha}\left|L_{m}\right\rangle\end{aligned} \tag{S51}$$

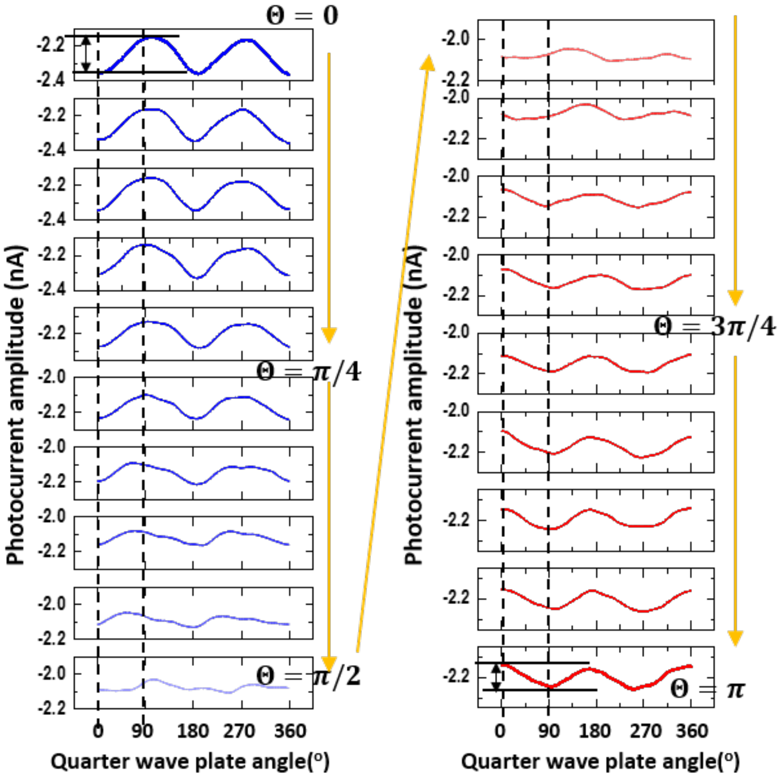

Figure S14: Photocurrent data as a function of the quarter wave plate angle, from a set of states: from P1 to P5, P5 to P2 on the HOPS.

Then, the new state becomes

$$|\psi\rangle = a_1 \left|L'_{-m}\right\rangle + a_2 \left|R'_{m}\right\rangle \tag{S52}$$

$j^{(\phi)}_{OPGE,\phi}$(Eqn. S43) now becomes,

$$\begin{aligned} & j^{(\phi)'}_{OPGE,\phi} \\ & = \frac{m}{\rho}|E_0|^2[\sigma(\gamma_{\phi\rho\phi\phi} + \gamma_{\rho\phi\phi\phi})\cos{(\Phi + 2(m+\sigma)\phi + 4\alpha_{hwp})} \\ & + (-\gamma_{\rho\rho\rho\rho} + \sigma^2\gamma_{\phi\phi\phi\phi})\sin{(\Phi + 2(m+\sigma)\phi + 4\alpha_{hwp})}]\sin\Theta \end{aligned} \tag{S53}$$

while the $j^{(0)}_{OPGE,\phi}$ part remains unchanged. From the expressions of $j^{(0)'}$ and $j^{(\phi)'}$, it can seen that only $j^{(\phi)'}$ can be modulated by the HWP, and its dependence on HWP angle α_{hwp} has a $\pi/2$ period. Hence, measuring the part of photocurrent that has a $\pi/2$ period when HWP rotates, is equivalent to measuring $j^{(\phi)}$. Furthermore, due to the $\cos{(\Phi + 2(m+\sigma)\phi + 4\alpha_{hwp})}$ dependence of $j^{(\phi)'}$, if a set of state $|\Psi\rangle\,|_{(\Theta,\Phi)}$ have same Θ coordinate, or in other words, a state winds on a latitude of the HOPS, and if photocurrent measurement is taken at a certain ϕ azimuthal angle, the total angle $\Phi + 4\alpha_{hwp}$ would determine the relative ’phase’ of the photocurrent. To be more precise,

$$\Delta\Phi = -4\Delta\alpha_{hwp} \tag{S54}$$

In our measurement, when changing the optical state from P3 to P5, from P5 to P4, $\Delta\Phi = \pi$, the photocurrent fitted by $J = J_l \sin{(4\alpha_{hwp} + \alpha_0)} + J_0$ had a change in ’phase’ α_0 by π (plotted in Fig. 3d in the main text), again confirming the existence of $j^{(\phi)}_{OPGE,\phi}$, and its dependence on Φ coordinate of states on HOPS. The full dependence of photocurrent on α_{hwp} is shown in Fig. S15.

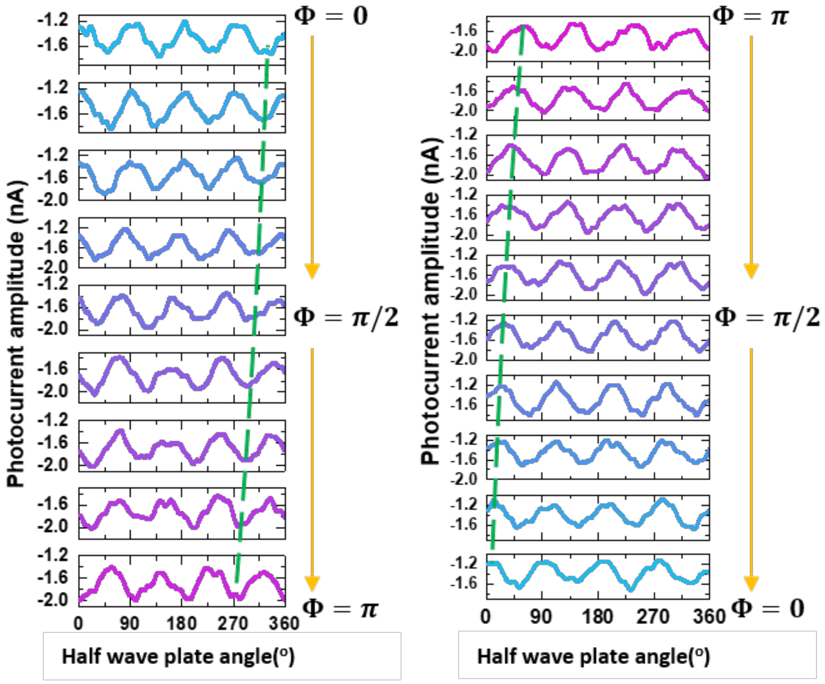

Figure S15: Photocurrent data as a function of the half wave plate angle, from a set of states on the equator of the HOPS: P3 to P5 to P4, then P4 to P3 (the other half circle).

3 Further demonstration of the existence of OPGE current

3.1 Eliminating sample related inhomogeneities

The edges of the exfoliated samples inherently have lower symmetries (i.e., $\mathrm{C_s}$ symmetry). In all the measurements described in the main paper, the laser beam shining on the $\mathrm{WTe_2}$ flake had a width similar to the electrodes separation, and was kept far away from all sample edges to avoid edge effects.

In order to further check whether the sample had intrinsic symmetry breaking due to defects or inhomogeneities, a Gaussian beam was de-focused to a spot size $\sim$ 100um (much larger than the sample sizes). In this case, the beam could be regarded as a plane wave and the regular photogalvanic effect can be studied, which could effectively reflect the symmetry reductions on the sample flake.

The photocurrent data as a function of quarter wave plate angle was plotted in Fig. S16. During many periods of rotation of the quarter wave plate, there was no apparent polarization dependence of photocurrent beyond the noise level (as expected). The absence of polarization dependent photocurrent rules out the contribution from sample imperfections (edge effects, defects).

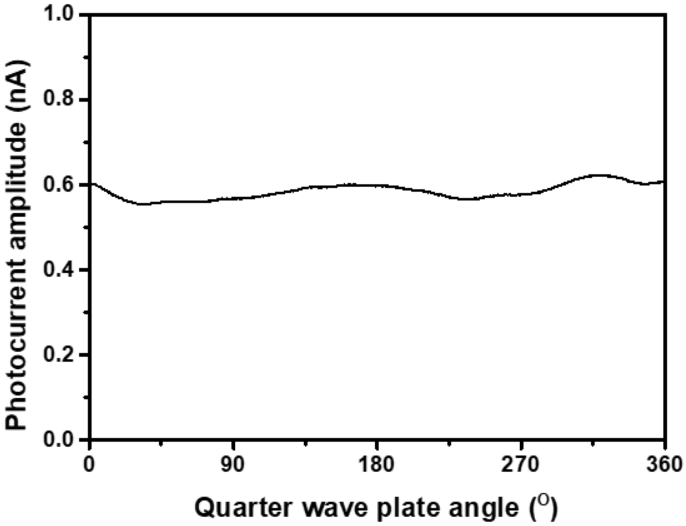

Figure S16: Photocurrent under nearly plane wave incidence (spot size $\sim$ 100 um).

3.2 Eliminating artifacts related to the optical beam

In order to differentiate the helical phase induced OPGE currents from the intensity gradient induced s-PGE currents (and also radial photon momentum in Gaussian beams, which is negligible in our measurements near focal plane), we always chose OAM +m and -m for comparison, two beams with a same intensity gradient but opposite helical phases. In our experiments, changing the beam from OAM +m to -m was achieved by switching the phase pattern on the spatial light modulator screen to its mirror image. As a result, the +m and -m beam profiles were guaranteed to be mirror symmetric to each other. When a beam carrying OAM +m is perfectly aligned and normally incident onto the sample, its intensity profile would have a full rotation symmetry, and changing its OAM number to -m would not change this intensity profile. However, due to the limited pixel number in the spatial light modulator, and the beam alignment may not be perfect, there can be a slight change in the intensity profile from OAM +m to -m beams and consequently, it may affect the amplitude of photocurrents.

To figure out whether the beam profile imperfections, which can break either the mirror symmetry or two fold rotational symmetries with respect to its beam axis, was contributing to the OPGE current, we designed two experiments; First, we patterned two pairs electrodes being '$\cup$' shaped and '$\cap$'(reversed '$\cup$') shaped on a same flake (Fig. S17a), and OAM +4 and -4 beams were incident onto the sample in sequence. Since both electrode pairs were on a same sample flake, the crystal-axes dependent OPGE conductivity coefficients were the same in both measurements. They collect a integral of OPGE current from either the top half semicircle or the bottom half semicircle. There are two possibilities:

1. Extrinsic effects (Fig. S17b): Assume that for OAM +4 beam, it has an intensity gradient $\vec{g}$ from its top to bottom, then for OAM -4 beam, due to the mirror reflection, it should have an intensity gradient $-\vec{g}$ from its bottom to its top. Since the light alignment was fixed in the whole measurement, and the direction of $\boldsymbol{J}_{OPGE}$ is correlated with the gradient vector $\vec{g}$, $\boldsymbol{J}_{OPGE}$ would adopt a same direction on both the '$\cup$' shaped device, and the '$\cap$' shaped device. This can be generalized to OAM beams with random gradients, where the difference between OPGE currents from OAM +m and -m ($\mathrm{J}_{\mathrm{OPGE}}^{+\mathrm{m}} - \mathrm{J}_{\mathrm{OPGE}}^{-\mathrm{m}}$), should have the same polarity for both devices.

2. Intrinsic effects (Fig. S17c): The phase gradients at the top and the bottom of the OAM beam have opposite signs, so that $\boldsymbol{J}_{OPGE}$ would flip its direction from the top point to the bottom point. Hence, the net current collected by the ' $\cup$' shaped and the '$\cap$' shaped electrodes should be both from the inside electrode to the outside electrode (or vice versa).

As shown in Fig. S18(b, c), the photocurrents from OAM +4 and -4 beams measured by device 1 and device 2 both showed opposite OPGE currents, confirming the existence of OPGE. Furthermore, the OPGE current from the same beam had different polarities on device 1 and 2. In other words, the OPGE current was flowing from the inside electrode to the outside electrode on both devices. Therefore, it opposes the symmetry analysis of an artificial intensity gradient induced current.

Having considered the possibility of the mirror symmetry breaking of OAM beams, we also examined the 2-fold rotation symmetry. A similar experiment was done using the 'Angular bracket' shaped electrodes. Two measurements were carried out with a same alignment of

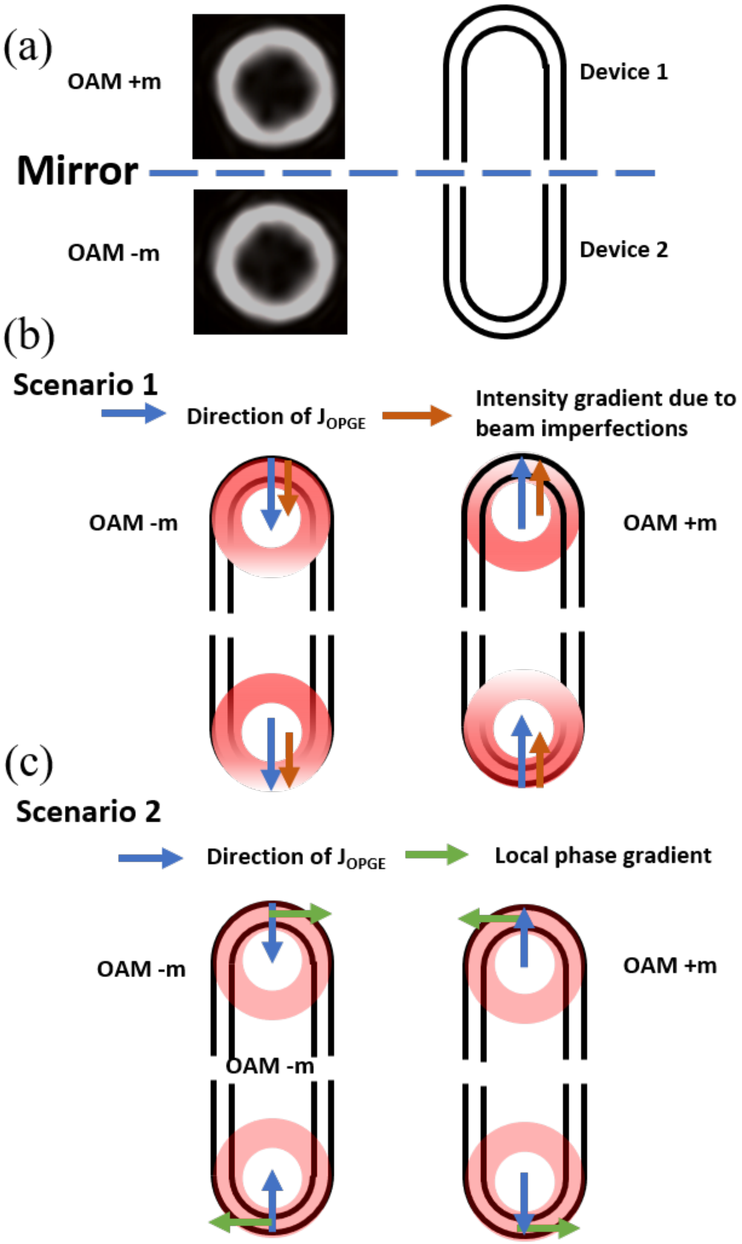

Figure S17: Schematics of the experiment design and two possibilities of the photocurrent from OAM beams. (a) The CCD images of optical beams with OAM +m and -m, and schematics of ∩ and ∪ shaped devices. (b and c) Schematics showing predicted directions of 'OPGE current' collected by the two devices, as denoted by the blue arrows.

the optical beam, but with the $\mathrm{WTe_2}$ sample flipped in-plane by $180°$. Ideally, with respect to the beam center, the system would maintain its C_{2v} symmetry, and this $180°$ flip would cause a flip in OPGE current as well. Otherwise, if the current is caused by some undesired intensity

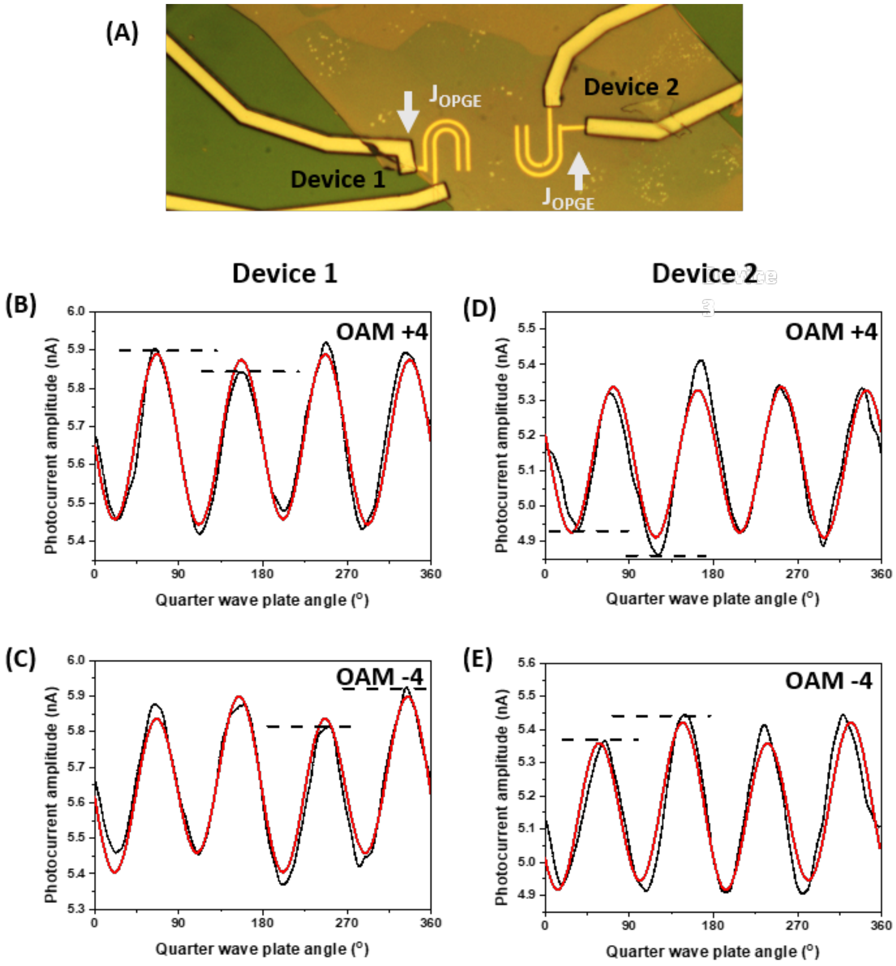

Figure S18: Photocurrent measured from '∩' and '∪' shaped devices on a same WTe_2 flake.

inhomogeneities of light due to nonideal alignment, its direction should be also random.

As shown in Fig. S19 (c-f) The photocurrent from OAM +4 and -4 measured before and after the flip of WTe_2 sample both showed opposite OPGE currents, confirming the existence of OPGE. Moreover, the OPGE current was flowing from the inside electrode to the outside electrode in both devices, indicating a polarity flip. Therefore, these measurements rules out the optical beam alignment induced artifacts.

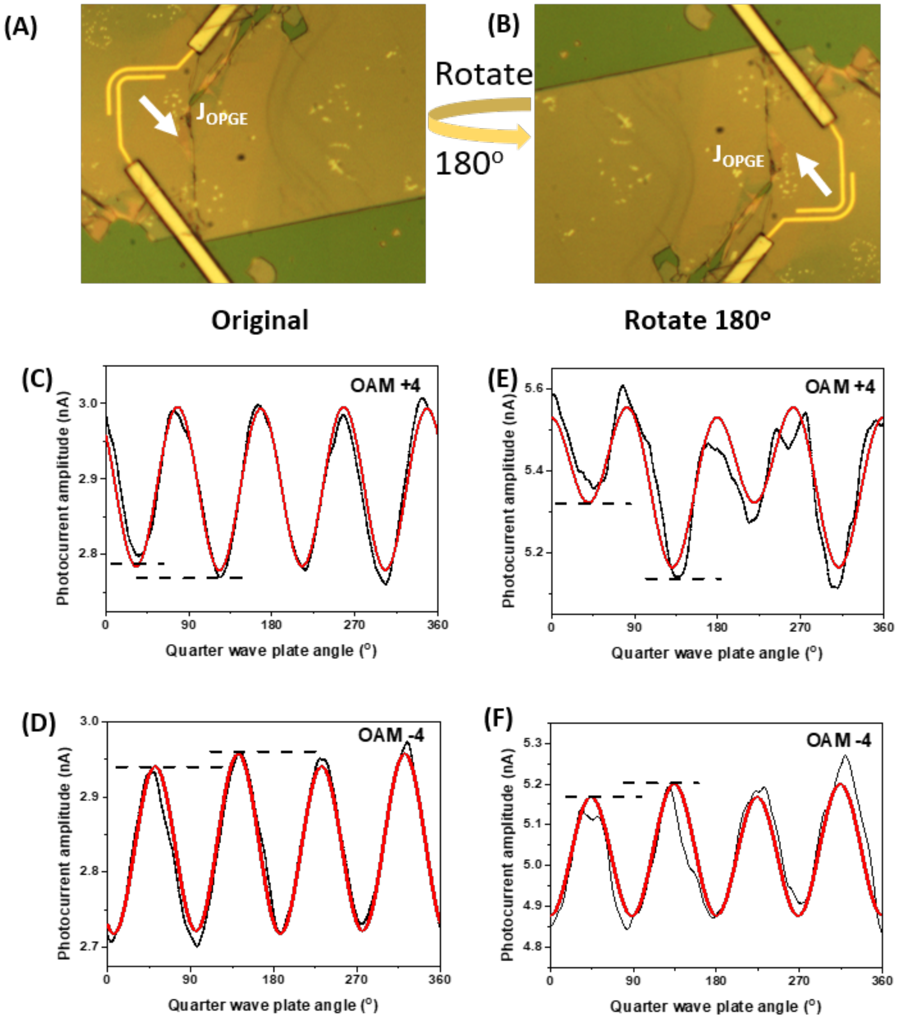

Figure S19: Photocurrent measured from two 'Angular bracket' shaped devices before and after a 180° in-plane rotation of the WTe_2 sample flake while keeping the optical alignment unchanged.

References and Notes

1. E. Ivchenko, S. Ganichev, *Optical Spectroscopy of Semiconductor Nanostructures* (Springer, 2008).

2. J. Sipe, A. Shkrebtii, Second-order optical response in semiconductors. *Phys. Rev. B* **61**, 5337–5352 (2000). doi:10.1103/PhysRevB.61.5337

3. S. Dhara, E. J. Mele, R. Agarwal, Voltage-tunable circular photogalvanic effect in silicon nanowires. *Science* **349**, 726–729 (2015). doi:10.1126/science.aac6275 Medline

4. L. Allen, M. W. Beijersbergen, R. J. Spreeuw, J. P. Woerdman, Orbital angular momentum of light and the transformation of Laguerre-Gaussian laser modes. *Phys. Rev. A* **45**, 8185–8189 (1992). doi:10.1103/PhysRevA.45.8185 Medline

5. L. Allen, M. Padgett, M. Babiker, in *Progress in Optics* (Elsevier, 1999), vol. 39, pp. 291–372.

6. P. Miao, Z. Zhang, J. Sun, W. Walasik, S. Longhi, N. M. Litchinitser, L. Feng, Orbital angular momentum microlaser. *Science* **353**, 464–467 (2016). doi:10.1126/science.aaf8533 Medline

7. C.-W. Qiu, Y. Yang, Vortex generation reaches a new plateau. *Science* **357**, 645 (2017). doi:10.1126/science.aan6359 Medline

8. Y. Chen, J. Gao, Z.-Q. Jiao, K. Sun, W.-G. Shen, L.-F. Qiao, H. Tang, X.-F. Lin, X.-M. Jin, Mapping Twisted Light into and out of a Photonic Chip. *Phys. Rev. Lett.* **121**, 233602 (2018). doi:10.1103/PhysRevLett.121.233602 Medline

9. G. C. Berkhout, M. P. Lavery, J. Courtial, M. W. Beijersbergen, M. J. Padgett, Efficient sorting of orbital angular momentum states of light. *Phys. Rev. Lett.* **105**, 153601 (2010). doi:10.1103/PhysRevLett.105.153601 Medline

10. C. Schulze, A. Dudley, D. Flamm, M. Duparre, A. Forbes, Measurement of the orbital angular momentum density of light by modal decomposition. *New J. Phys.* **15**, 073025 (2013). doi:10.1088/1367-2630/15/7/073025

11. M. G. Mandujano, J. A. Maytorena, Quadrupolar second-harmonic generation by helical beams and vectorial vortices with radial or azimuthal polarization. *Phys. Rev. A* **88**, 023811 (2013). doi:10.1103/PhysRevA.88.023811

12. G. F. Quinteiro, D. Reiter, T. Kuhn, Formulation of the twisted-light–matter interaction at the phase singularity: The twisted-light gauge. *Phys. Rev. A* **91**, 033808 (2015). doi:10.1103/PhysRevA.91.033808

13. K. Shintani, K. Taguchi, Y. Tanaka, Y. Kawaguchi, Spin and charge transport induced by a twisted light beam on the surface of a topological insulator. *Phys. Rev. B* **93**, 195415 (2016). doi:10.1103/PhysRevB.93.195415

14. G. Walker, A. S. Arnold, S. Franke-Arnold, Trans-spectral orbital angular momentum transfer via four-wave mixing in Rb vapor. *Phys. Rev. Lett.* **108**, 243601 (2012). doi:10.1103/PhysRevLett.108.243601 Medline

15. C. T. Schmiegelow, J. Schulz, H. Kaufmann, T. Ruster, U. G. Poschinger, F. Schmidt-Kaler, Transfer of optical orbital angular momentum to a bound electron. *Nat. Commun.* **7**, 12998 (2016). doi:10.1038/ncomms12998 Medline

16. N. Clayburn, J. L. McCarter, J. M. Dreiling, M. Poelker, D. M. Ryan, T. J. Gay, Search for spin-polarized photoemission from GaAs using light with orbital angular momentum. *Phys. Rev. B* **87**, 035204 (2013). doi:10.1103/PhysRevB.87.035204

17. D. L. Andrews, *Structured Light and Its Applications: An Introduction to Phase-Structured Beams and Nanoscale Optical Forces* (Academic Press, 2011).

18. K. Dholakia, N. B. Simpson, M. J. Padgett, L. Allen, Second-harmonic generation and the orbital angular momentum of light. *Phys. Rev. A* **54**, R3742–R3745 (1996). doi:10.1103/PhysRevA.54.R3742 Medline

19. Materials and methods are available as supplementary materials.

20. A. A. Soluyanov, D. Gresch, Z. Wang, Q. Wu, M. Troyer, X. Dai, B. A. Bernevig, Type-II Weyl semimetals. *Nature* **527**, 495–498 (2015). doi:10.1038/nature15768 Medline

21. Z. Ji, G. Liu, Z. Addison, W. Liu, P. Yu, H. Gao, Z. Liu, A. M. Rappe, C. L. Kane, E. J. Mele, R. Agarwal, Spatially dispersive circular photogalvanic effect in a Weyl semimetal. *Nat. Mater.* **18**, 955–962 (2019). doi:10.1038/s41563-019-0421-5 Medline

22. G. B. Osterhoudt, L. K. Diebel, M. J. Gray, X. Yang, J. Stanco, X. Huang, B. Shen, N. Ni, P. J. W. Moll, Y. Ran, K. S. Burch, Colossal mid-infrared bulk photovoltaic effect in a type-I Weyl semimetal. *Nat. Mater.* **18**, 471–475 (2019). doi:10.1038/s41563-019-0297-4 Medline

23. F. de Juan, A. G. Grushin, T. Morimoto, J. E. Moore, Quantized circular photogalvanic effect in Weyl semimetals. *Nat. Commun.* **8**, 15995 (2017). doi:10.1038/ncomms15995 Medline

24. S. M. Young, A. M. Rappe, First principles calculation of the shift current photovoltaic effect in ferroelectrics. *Phys. Rev. Lett.* **109**, 116601 (2012). doi:10.1103/PhysRevLett.109.116601 Medline

25. J. L. Cheng, N. Vermeulen, J. E. Sipe, Second order optical nonlinearity of graphene due to electric quadrupole and magnetic dipole effects. *Sci. Rep.* **7**, 43843 (2017). doi:10.1038/srep43843 Medline

26. J. Karch, C. Drexler, P. Olbrich, M. Fehrenbacher, M. Hirmer, M. M. Glazov, S. A. Tarasenko, E. L. Ivchenko, B. Birkner, J. Eroms, D. Weiss, R. Yakimova, S. Lara-Avila, S. Kubatkin, M. Ostler, T. Seyller, S. D. Ganichev, Terahertz radiation driven chiral edge currents in graphene. *Phys. Rev. Lett.* **107**, 276601 (2011). doi:10.1103/PhysRevLett.107.276601 Medline

27. Z. Shao, J. Zhu, Y. Chen, Y. Zhang, S. Yu, Spin-orbit interaction of light induced by transverse spin angular momentum engineering. *Nat. Commun.* **9**, 926 (2018). doi:10.1038/s41467-018-03237-5 Medline

28. C. Maurer, A. Jesacher, S. Fürhapter, S. Bernet, M. Ritsch-Marte, Tailoring of arbitrary optical vector beams. *New J. Phys.* **9**, 78 (2007). doi:10.1088/1367-2630/9/3/078

29. G. Milione, H. I. Sztul, D. A. Nolan, R. R. Alfano, Higher-order Poincaré sphere, stokes parameters, and the angular momentum of light. *Phys. Rev. Lett.* **107**, 053601 (2011). doi:10.1103/PhysRevLett.107.053601 Medline

30. D. Naidoo, F. S. Roux, A. Dudley, I. Litvin, B. Piccirillo, L. Marrucci, A. Forbes, Controlled generation of higher-order Poincaré sphere beams from a laser. *Nat. Photonics* **10**, 327–332 (2016). doi:10.1038/nphoton.2016.37